

A_{2B} adenosine receptor antagonists rescue lymphocyte activity in adenosine-producing patient-derived cancer models

Apple Hui Min Tay ^{1,2}, Rubén Prieto-Díaz,³ Shiyong Neo,^{2,4} Le Tong,² Xinsong Chen ², Valentina Carannante,^{5,6} Björn Önfelt,^{5,6} Johan Hartman,^{2,7} Felix Haglund,^{2,7} Maria Majellaro,⁸ Jhonny Azaque,³ Xerardo Garcia-Mera,³ Jose M Brea,⁸ Maria I Loza,⁸ Willem Jespers,⁹ Hugo Gutierrez-de-Teran ¹⁰, Eddy Sotelo,³ Andreas Lundqvist ²

To cite: Tay AHM, Prieto-Díaz R, Neo S, *et al.* A_{2B} adenosine receptor antagonists rescue lymphocyte activity in adenosine-producing patient-derived cancer models. *Journal for ImmunoTherapy of Cancer* 2022;**10**:e004592. doi:10.1136/jitc-2022-004592

► Additional supplemental material is published online only. To view, please visit the journal online (<http://dx.doi.org/10.1136/jitc-2022-004592>).

AHMT and RP-D contributed equally.

ES and AL are joint senior authors.

Accepted 26 April 2022



© Author(s) (or their employer(s)) 2022. Re-use permitted under CC BY. Published by BMJ.

For numbered affiliations see end of article.

Correspondence to

Dr Andreas Lundqvist;
Andreas.Lundqvist@ki.se

Dr Eddy Sotelo; e.sotelo@usc.es

ABSTRACT

Background Adenosine is a metabolite that suppresses antitumor immune response of T and NK cells via extracellular binding to the two subtypes of adenosine-2 receptors, A₂ARs. While blockade of the A_{2A}ARs subtype effectively rescues lymphocyte activity, with four A_{2A}AR antagonists currently in anticancer clinical trials, less is known for the therapeutic potential of the other A_{2B}AR blockade within cancer immunotherapy. Recent studies suggest the formation of A_{2A}AR/A_{2B}AR dimers in tissues that coexpress the two receptor subtypes, where the A_{2B}AR plays a dominant role, suggesting it as a promising target for cancer immunotherapy.

Methods We report the synthesis and functional evaluation of five potent A_{2B}AR antagonists and a dual A_{2A}AR/A_{2B}AR antagonist. The compounds were designed using previous pharmacological data assisted by modeling studies. Synthesis was developed using multicomponent approaches. Flow cytometry was used to evaluate the phenotype of T and NK cells on A_{2B}AR antagonist treatment. Functional activity of T and NK cells was tested in patient-derived tumor spheroid models.

Results We provide data for six novel small molecules: five A_{2B}AR selective antagonists and a dual A_{2A}AR/A_{2B}AR antagonist. The growth of patient-derived breast cancer spheroids is prevented when treated with A_{2B}AR antagonists. To elucidate if this depends on increased lymphocyte activity, immune cells proliferation, and cytokine production, lymphocyte infiltration was evaluated and compared with the potent A_{2A}AR antagonist AZD-4635. We find that A_{2B}AR antagonists rescue T and NK cell proliferation, IFN γ and perforin production, and increase tumor infiltrating lymphocytes infiltration into tumor spheroids without altering the expression of adhesion molecules.

Conclusions Our results demonstrate that A_{2B}AR is a promising target in immunotherapy, identifying ISAM-R56A as the most potent candidate for A_{2B}AR blockade. Inhibition of A_{2B}AR signaling restores T cell function and proliferation. Furthermore, A_{2B}AR and dual A_{2A}AR/A_{2B}AR antagonists showed similar or better results than A_{2A}AR antagonist AZD-4635 reinforcing the idea of dominant role of the A_{2B}AR in the regulation of the immune system.

WHAT IS ALREADY KNOWN ON THIS TOPIC

⇒ A_{2B}AR is a low affinity adenosine receptor that is activated by high adenosine concentration. With adenosine being an anti-inflammatory and immunosuppressive metabolite that accumulates at high concentrations in the tumor microenvironment, targeting A_{2B}AR is a promising metabolic immune checkpoint.

WHAT THIS STUDY ADDS

⇒ We synthesized high affinity non-xanthine A_{2B}AR antagonists with improved T and NK cell activities under exogenous and endogenous adenosine suppression. A_{2B}AR inhibition furthermore improves infiltration of tumor-infiltrating lymphocytes into patient-derived 3D spheroids.

HOW THIS STUDY MIGHT AFFECT RESEARCH, PRACTICE AND/OR POLICY

⇒ These findings provide practical readouts to study adenosine-mediated suppression and identified putative A_{2B}AR antagonists to alleviate suppression of T and NK cells.

BACKGROUND

Accounting for its heterogeneity with more than 100 distinct types, cancer is a complex and dynamic disease.¹ This complexity has been rationalized to 10 transforming hallmarks, of which avoiding immune destruction explains how the immune system plays an essential role during tumorigenesis.¹ Therapies based on activating the immune system can result in beneficial responses in patients with metastatic cancer.² Treatment with antibodies targeting the immunological checkpoint axis PD-1–PD-L1/2 can result in potent antitumor T cell activation and clinically meaningful long-lasting responses.² Primary resistance to immune checkpoint

therapy can be attributed to the absence of intratumoral T cells. This has fueled the search for strategies to convert immune-excluded tumors to immune-infiltrated tumors.² Since the tumor microenvironment (TME) often imposes metabolic stress and dysregulation on tumor infiltrating lymphocytes (TILs), targeting immune metabolism represents a promising direction.³

Purinergic signaling involves extracellular purine nucleosides [Adenosine (ADO)] and nucleotides (ATP and AMP) as signaling molecules. ADO, an ubiquitous metabolite with critical anti-inflammatory and immunosuppressive roles, downregulates inflammatory cytokine secretion as well as decreases the effector function and proliferation of T and natural killer (NK) cells (online supplemental figure 1).⁴ Several tumors display transformed purine metabolism thereby facilitating the production of ADO and reducing its degradation.⁵ Oxygen deprivation reduces the availability of energy source and promotes the accumulation of extracellular ATP.⁶ Moreover, hypoxia is a strong inducer of the ectonucleotidases CD39 and CD73.⁴ The released ATP suffers the consecutive action of these ectonucleotidases resulting in increased ADO concentration from nanomolar (nM) in physiological conditions to micromolar (μ M) range in the TME.^{7–10}

Extracellular ADO binds to purinergic type-1 G-protein coupled receptors (GPCRs), accordingly named adenosine receptors (AR)—A₁AR, A_{2A}AR, A_{2B}AR and A₃AR.^{4,11} A_{2A}AR is highly expressed in most immune cells, with evidences supporting that its activation in the TME suppresses antitumor immune responses,^{12–13} enhancement of regulatory T cells immune suppressive activity¹⁴ and inhibition of antigen presentation by dendritic cells.¹⁵ These reports set the foundation for inhibiting A_{2A}AR in hypoxic tumors to improve antitumor immune responses. Consequently, A_{2A}AR antagonism has emerged as a prototypical approach of small molecule immunotherapeutic, with recent encouraging clinical outcomes in treatment-refractory cancer,^{16–17} along the four A_{2A}AR antagonists already in clinical trials.¹⁸

While the A₁AR, A_{2A}AR and A₃AR receptor subtypes bind ADO with high affinity, the A_{2B}AR exhibits a low affinity profile. Thus, A_{2B}AR will only be activated by high ADO concentrations which usually takes place under extreme environmental cues like inflammation, injury, hypoxia or cellular stress.^{19–20} Recent evidence suggests A_{2B}AR roles in cancer,^{5–21} following early studies highlighting its activation as a promoter for tumor proliferation,^{5–6} angiogenesis,²² cell invasion and metastasis.⁵ Furthermore, the presence of A_{2B}AR in mast cells, neutrophils, dendritic cells, macrophages and lymphocytes has shown important immunoregulatory roles within the immune suppressive TME.^{4–5,23} The expression and signaling of the two A₂AR subtypes are highly affected by pathological conditions, with the A_{2B}AR/A_{2A}AR expression ratio rapidly increasing under hypoxic conditions.^{5,19–24} In this context, a recent study demonstrated extensive heteromeric complex formation in tissues where A_{2B} and A_{2A} ARs were coexpressed.¹⁹ A_{2A}AR was previously shown to be involved in

regulation of A_{2B}AR cell surface expression.²⁵ Moreover, a dramatically altered pharmacology of the A_{2A}AR was observed when coexpressed with the A_{2B}AR with selective A_{2A}AR ligands loosing high affinity binding to A_{2A}AR and showing reduced potency. These would have major implications for the clinical use of A_{2A}AR ligands, as they would fail to modulate the receptor in an A_{2A}AR-A_{2B}AR heterodimer context. Instead, the A_{2A}AR-A_{2B}AR heterodimer and the A_{2B}AR could be considered as novel promising pharmacological targets for cancer immunotherapy.

In this study, six non-xanthinic A₂AR antagonists, five selective A_{2B}AR and a dual A_{2A}AR/A_{2B}AR, were evaluated for their immunomodulatory effect. Non-xanthinic scaffold exhibits improved pharmacokinetic properties and bring structural novelty to adenosine antagonists reported to date.^{26–27} Using healthy donor in vitro and patient-derived ex vivo models, we demonstrated that antagonizing A_{2B}AR signaling significantly alleviated adenosine-mediated suppression across different lymphocyte subsets. Notably, marked differences in the outcomes of A_{2B}AR antagonist drug screening were observed when comparing exogenous and endogenously produced ADO. These results show a comparative immunological footprint among different A_{2B}AR antagonists, a dual A_{2B}AR/A_{2A}AR antagonist and an A_{2A}AR antagonist in clinical trials, strongly suggesting that the A_{2B}AR is a promising target in cancer immunotherapy.

MATERIALS AND METHODS

Chemistry

The synthesis of the previously described antagonists, analytical procedure and spectroscopic and analytical data for all the compounds is detailed in online supplemental information. For the synthesis of ISAM-R56A, a mixture of isopropyl 4-(furan-2-yl)-2-methyl-1,4-dihydrobenzo^{4,5}imidazo[1,2-a]pyrimidine-3-carboxylate (ISAM-140) (1 mmol), 2-fluorobenzyl bromide (3 mmol) and potassium carbonate (4 mmol) in 4 mL of DMF was orbitally stirred in a coated Kimble vial at 80°C for 5 hours. After completion of the reaction, as indicated by TLC, the solvent was removed in vacuum and the obtained oily residue was purified by column chromatography on silica gel to obtain two regioisomers (ISAM-R56A and ISAM-R56B). For the synthesis of ISAM-M89A, a mixture of 2-amino-5-chlorobenzimidazole (7.5 mmol), 3-furanocarboxaldehyde (5 mmol), isopropyl acetoacetate (5 mmol) and ZnCl₂ (0.5 mmol) in 2.5 mL of THF was orbitally stirred in a coated Kimble vial at 80°C for 12 hours. After completion of the reaction, as indicated by TLC, the solvent was removed and the obtained oily residue was purified by column chromatography on silica gel, to obtain two regioisomers (ISAM-M89A and ISAM-M89B).

Binding affinity of adenosine receptor subtypes

The affinity and selectivity profiles of the ligands obtained was studied in vitro, radioligand binding assays, at the four

human specific ARs subtypes, using experimental protocols previously described.^{28–30} All ligands were prepared and tested as racemic mixtures. Human ARs expressed in transfected CHO (A₁AR), HeLa (A_{2A}AR and A₃AR) and HEK-293 (A_{2B}AR) cells were employed. The following radioligands were used for binding experiments: [³H]DPCPX for A₁AR and A_{2B}AR, at 2 and 25 nM, respectively; [³H]ZM241385 at 3 nM for A_{2A}AR; and [³H]NECA at 30 nM for A₃AR. Non-specific binding was determined in the presence of R-PIA 10 μM for A₁AR, NECA 50 μM for A_{2A}AR, NECA 400 μM for A_{2B}AR and R-PIA 100 μM for A₃AR. The biological data are expressed as K_i (nM, n=3). K_i values were obtained by fitting the data with non-linear regression using Prism 5.0 software (GraphPad, San Diego, CA, USA). Results are the mean of three experiments, each performed in duplicate.

Blockade of hCD73 assays

The selected AR antagonists were tested at 1 μM and 10 μM. Experiments (human CD73) were carried out in a white 384-Optiplate (Perkin Elmer 6007290). Test compounds and the standard (α-β-methylene adenosine, Sigma M3763), 0.5 μg/mL enzyme (Cayman RYD-5795-EN-010), 300 μM AMP (Sigma A2252) and 100 μM ATP (A2383) were added in a final volume of 25 μL/well, using 25 mM Tris-HCl, 5 mM MgCl₂·6H₂O, pH=7.4 as assay buffer. The reaction mixture was incubated at 37°C for 15 min, after incubation 25 μL of Cell Titer-Glo Luminescent cell viability (Promega G7571) was added and shaken during 2 min before incubation at RT for 10 min. Luminescence at 100 ms was measured in the Perkin Elmer Enspire multimode plate reader.

cAMP assays

Assays were performed in transfected A_{2B}AR using a cyclic AMP (cAMP) enzyme immunoassay kit (Amersham Biosciences) following previously described protocols.^{28,30} HEK-293 cells were seeded (10,000 cells/well) in 96-well culture plates and incubated at 37°C in an atmosphere with 5% CO₂ in Eagle's Medium Nutrient Mixture F-12 (EMEM F-12), containing 10% fetal calf serum (FCS) and 1% L-Glutamine. Cells were washed three times with 200 μL assay medium (EMEM-F12 and 25 mM HEPES pH=7.4) and pre-incubated with assay medium containing 30 μM rolipram and test compounds at 37°C for 15 min. Ten μM NECA was incubated for 15 min at 37°C (total incubation time 30 min). Reaction was stopped with lysis buffer supplied in the kit and the enzyme immunoassay was carried out for detection of intracellular cAMP at 450 nm in an Ultra Evolution detector (Tecan). The dose-response curve of NECA-elicited cAMP formation was used to determine the initial choice of A_{2B}AR antagonist concentration (online supplemental figure 2).

Computational modeling

A previously reported model of the A_{2B}AR in complex with the reference antagonist ISAM-140 was the starting point to investigate the binding mode of the antagonists here

reported.³¹ Briefly, the inactive hA_{2B}AR conformation was generated by homology modeling based on curated alignment with the A_{2A}AR, of known structure, followed by some refinement steps as previously described.^{28,32} The initial binding orientation of ISAM-140, initially obtained by automated docking with GOLD,³⁰ was herein refined with a round of MD simulations, consisting of: (i) insertion of the A_{2B}AR-ISAM-140 complex on an atomistic model of the membrane, solvation, and a 5 ns MD equilibration protocol as implemented in the PyMemDyn module of the GPCR-ModSim webserver;³³ (ii) a short MD equilibration of the binding site, consisting on a 25 Å radius solvated sphere with the software Q³⁴ as detailed in online supplemental information. The remaining ligands were modeled in the equivalent stereoisomer and aligned with the 'Flexible Ligand Superposition' in Schrödinger³⁵ to this pose of ISAM-140. Each complex was subject to the same MD equilibration of the binding site outlined for ISAM-140, with representative snapshots shown in figure 1C.

PBMC and immune cell isolation

Peripheral blood mononuclear cells (PBMCs) were isolated from healthy blood donors' buffy coat and patient's blood after Ficoll density gradient centrifugation (GE Healthcare). NK cells were isolated using MACS MicroBead Human NK cell isolation kit (Miltenyi Biotec).

Tumor tissue processing and cell lines

Fresh tumor tissue resections were digested and processed into single cell suspension using gentleMACS tumor dissociation kit (Miltenyi Biotec). Tumor cells were then isolated by negative selection using a tumor cell isolation kit (Miltenyi Biotec). Adherent cells were passaged at least five times before being used for experiments. All cell lines were maintained in RPMI 1640 or DMEM GlutaMAX media (Thermo Fisher Scientific) supplemented with 10% HyClone fetal bovine serum (FBS) (GE Healthcare) and 1% Penicillin Streptomycin (PS) (Life Technologies). A tumor cell line and TIL culture from a breast cancer specimen was established as previously described.³⁶ Human osteosarcoma cell line U2OS (ATCC) was used in comparison to patient-derived sarcoma cell lines for relative adenosine production and ADO ectonucleotidase expression by flow cytometry.

Expansion of tumor infiltrating lymphocytes

Digested tumor resections were cultured in suspension with 5% human serum in AIM-V (Thermo Fisher Scientific) or X-VIVO20 (Lonza) media supplemented with 3000 IU/mL of IL-15 (Novartis). After 7 days, irradiated PBMCs (100 Gy) pooled from at least three healthy donors were added as feeder cells at 200:1 ratio with addition of anti-CD3 functional grade antibody and 500 IU/mL of IL-15. After an additional 10 days of culture, TILs were harvested and analyzed for purity using flow cytometry and maintained with 500 IU/mL of IL-15.

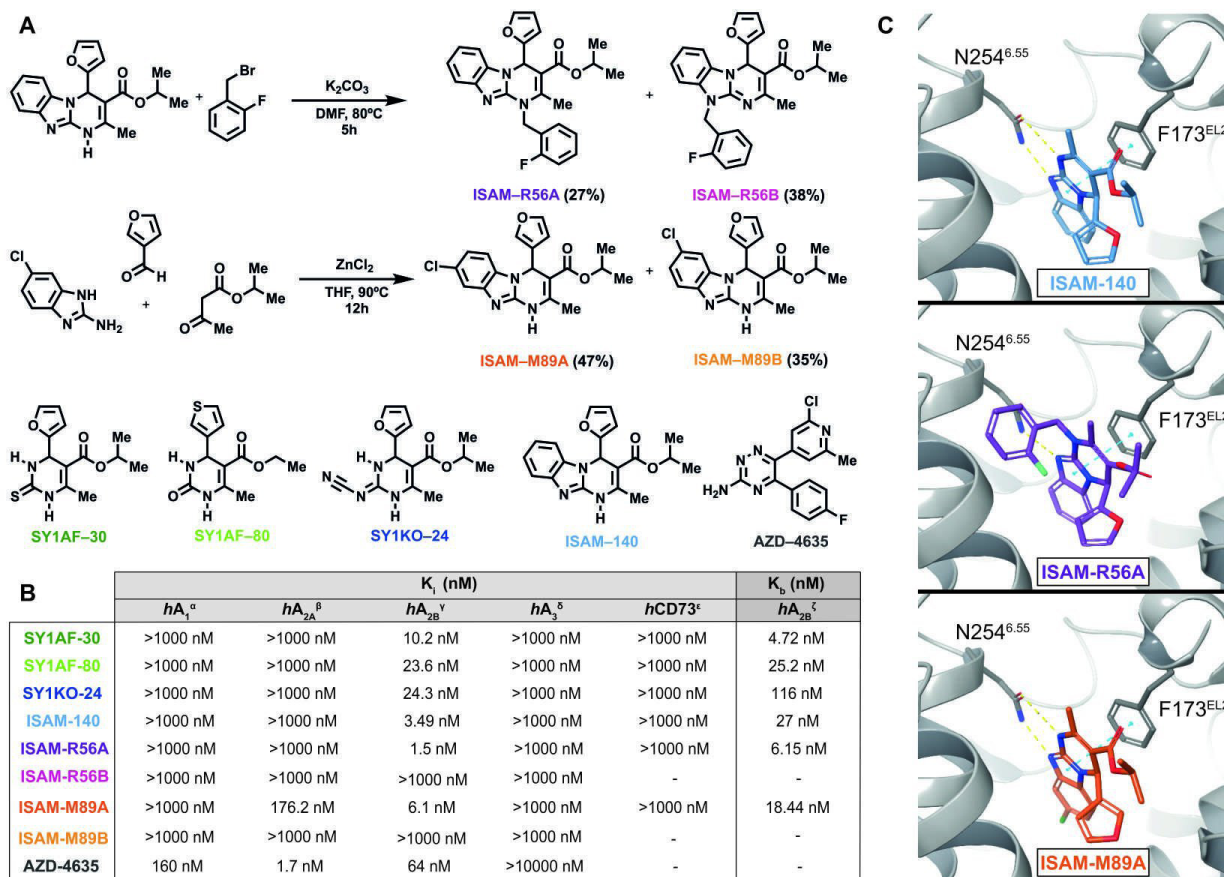


Figure 1 Pyrimidine derivatives as potent and highly selective A_{2B} AR antagonists. (A) Synthesis of the novel A_{2B} AR antagonist (ISAM-R56A) and the dual A_{2A} AR/ A_{2B} AR antagonist (ISAM-M89A) and structure of four A_{2B} AR antagonists previously published and the A_{2A} AR clinical candidate (AZD-4635) employed in the study.^{17,26-28} (B) Adenosine receptors binding data, A_{2B} AR functional data and $hCD73$ inhibitory data of the A_{2B} AR antagonists employed in the study. ^{α} Displacement of specific [³H] DPCPX binding in human CHO cells expressed as K_i in nM (n=3). ^{β} Displacement of specific [³H]4-(2-[7-amino-2-(2-furyl)^{1,2,4} triazolo[2,3-a]^{1,3,5} triazin-5-ylamino]ethyl)phenol binding in human HeLa cells expressed as K_i in nM (n=3). ^{γ} Displacement of specific [³H]DPCPX binding in human HEK-293 cells expressed as K_i in nM (n=3). ^{δ} Displacement of specific [³H]NECA binding in human HeLa cells expressed as K_i in nM (n=3). ^{ϵ} Inhibition of $hCD73$ in presence of α - β -methylene adenosine, ATP and AMP (expressed as K_i in nM). ^{ζ} cAMP production in HEK-293 cells in presence of NECA and test compound at a concentration of 10 μ M expressed as K_b in nM (n=3) (concentration-response curves shown in online supplemental figure 1). (C) Binding mode of the three most potent compounds disclosed in this study. All three compounds interact with N254^{6,55} and F173^{EL2}, both of which are crucial in AR ligand recognition. Up: ISAM-140 (light blue), center: ISAM-R56A (purple) only forms one hydrogen bond with N254^{6,55}, but additionally explores a pocket between TM6 and TM7, down: ISAM-M89A (orange), where the Cl atom (green stick) protrudes deep in the binding pocket.

Cell viability assay (Cell-Titer Glo)

From breast cancer single cell suspension, 3×10^3 cells were seeded and cultured in an ultra-low attachment 384-well plate (Corning) with DMEM-F12 media (Thermo Fisher Scientific) containing 20% FBS and 1% PS. Treatment with A_{2B} AR antagonist at various concentrations are stated in the Results section. After 4 days, Cell-Titer Glo reagent (Promega) was used to measure cell viability in accordance to the manufacturer's instruction. EnSpire Multilabel Reader (PerkinElmer) was used to read the luminescence.

Proliferation assay with exogenous adenosine

Freshly isolated PBMCs and NK cells were stained with 5 μ M FITC-conjugated carboxyfluorescein succinimidyl ester (CFSE, BioLegend) in phosphate-buffered saline

(PBS) (Life Technologies) at room temperature for 5 min. CFSE stained cells were washed with flow cytometer buffer three times. CFSE-labeled healthy PBMCs and NK cells were cultured in 96-well plates with X-VIVO20% and 1% PS for 3 and 6 days, respectively. Healthy PBMCs were incubated with Human T-activator CD3/CD28 beads at 1:4 ratio (Thermo Fisher Scientific) and IL-2 (Novartis) at 100 IU/mL. Healthy donor NK cells were incubated with 1000 IU/mL IL-2 only. 2×10^5 PBMCs and 5×10^4 NK cells were counted for treatment with ADO (Sigma-Aldrich) and 12 μ M of A_{2B} AR antagonist at the same day.

Proliferation assay with CD73-expressing patient-derived sarcoma spheroid

A malignant peripheral nerve sheath tumor (MPNST) patient-derived sarcoma cell line was used to grow

spheroid by seeding 1×10^4 cells per well in a 96-well ultra-low attachment plate (Thermo Fisher Scientific) with DMEM-F12 media containing 20% FBS and 1% PS for 5 days. 1×10^5 CFSE-labeled healthy PBMCs, ratio of 10:1, were added to the CD73 expressing, adenosine-producing spheroid at day five. Similar to the proliferation assay with exogenous ADO, CD3/CD28 beads at 1:4 ratio and IL-2 at 100 IU/mL were added. A_{2B} AR antagonism treatment at 12 μ M was added at the same day.

Spheroid infiltration by autologous TILs

Spheroids were prepared using patient-derived sarcoma cell lines. 1×10^4 cells were seeded per well in 96-well ultra-low attachment plate with DMEM-F12 media containing 20% FBS and 1% PS for 5 days. 3×10^4 CFSE-labeled autologous expanded TILs, at Effector:target ratio of 3:1, were added to the spheroid at day five with A_{2B} AR antagonism treatment at 12 μ M. After 3 days, spheroid was removed and split into two groups—IN and OUT. IN indicates TILs infiltrated into the sphere, while OUT indicates TILs that did not infiltrate into the sphere. Spheroids were washed with PBS at least two times. GentleMACS tumor dissociation kit (Miltenyi Biotec) was used to digest the spheroids for FC analysis.

Real-time imaging

Brightfield and phase contrast images under 4X objective were acquired every 6 hours on IncuCyte S3 system (Essen BioScience). For breast cancer patient-derived spheroid culture, 1×10^4 cells per well were seeded with A_{2B} AR antagonist at 12 μ M treatment for 6 days real time imaging. For spheroid infiltration, after the addition of CFSE-labeled autologous expanded TILs and treatment with A_{2B} AR antagonist at 12 μ M, green fluorescence images were acquired for 3 days. All spheroid invasion analysis was performed using top hat segmentation with IncuCyte software.

Extracellular ADO uptake assay via pAMPK staining

Experimental setup was adopted from a previous study whereby AR antagonist was added to pretreat cells before exogenous adenosine treatment for intracellular and cytokine staining.³⁷ In brief, PBMCs were treated with 12 μ M of A_{2B} AR antagonists for 90 min before the addition of 50 μ M of adenosine for 2 hours. Cells were harvested after 3 hours of CD3/CD28 bead stimulation before intracellular staining with phosphor-AMPK (Thr183, Thr172) rabbit primary antibody (Thermo Fisher Scientific) and antirabbit secondary antibody (BD biosciences).

IFN γ and perforin cytokine production assay

Similar experimental setup was performed as the extracellular ADO uptake assay. Cells were harvested after 2 days of CD3/CD28 bead stimulation before treatment with PMA/ionomycin (Sigma Aldrich) and golgi-inhibitors (BD biosciences). After 3 hours of subsequent incubation, intracellular staining was performed for IFN γ and perforin (online supplemental table 1).

Flow cytometry analysis

Cell surface was stained with mouse monoclonal anti-human antibodies against CD3, CD4, CD8, CD45RA, CD56 and CD19 listed in online supplemental table 1. Cell surface antibodies and live/dead (L/D) marker were incubated with samples at 4°C for 20 min after washing two times with flow cytometry buffer containing 5% FBS in PBS. For spheroid infiltrated TIL phenotyping, digested IN and OUT spheroids were stained with cell surface marker and analyzed on NovoCyte (ACEA Bioscience) with the use of FlowJo software (Tree Star) by gating single cell based on forward and side scatters. A representative gating strategy for CD8 naïve T cells is shown in online supplemental figure 3A. Compensated flow cytometry standard (FCS) files with only live cells were concatenated for downstream tSNE analysis using the 'cytofkit' R package (<https://github.com/JinmiaoChenLab/cytofkit>).

Statistical analysis

Experimental replicates are presented as mean \pm SD and median in box plot stated in the figure legend of the result section. Statistical analysis was performed using Prism 8 (GraphPad Software) and stated in figure legends.

RESULTS

Synthesis and pharmacological characterization of potent A_{2B} AR antagonists

The pyrimidine derivatives studied here were obtained using a modified procedure of the reliable Biginelli reaction,³⁸ consisting of the catalyzed condensation of an aldehyde, a β -keto-ester and a 1,3-dinucleophile. The synthesis and binding data of SY1AF-30,²⁹ SY1AF-80,²⁹ SY1KO-24²⁸ and ISAM-140³⁰ (figure 1A) were recently described by our group in the context of a program to develop novel A_{2B} AR antagonists. In addition, we present two previously undisclosed derivatives (ISAM-R56A and ISAM-R89A, figure 1A). These compounds are structurally related to ISAM-140 and they were discovered in the context of the structure activity relationship (SAR) exploration and structural diversification of the tricyclic scaffold present in this prototypical A_{2B} AR antagonist. Besides providing distinctive and not-self-evident structural novelties, this pair of compounds offer interesting pharmacological data from quantitative (K_i in the low nM range) and qualitative (dual profile) points of view.

The synthetic pathway employed to prepare the novel A_{2B} AR ligands is shown in figure 1A, where it can be observed that both transformations exploit the tautomerism present in the precursors. Briefly, treatment of ISAM-140 with 2-fluorobenzyl bromide under basic conditions produced a mixture of regioisomers (ISAM-R56A and ISAM-R56B) that was separated using column chromatography. The Biginelli-inspired $ZnCl_2$ -catalyzed condensation of 2-amino-5-chlorobenzimidazole, 3-furanocarboxaldehyde and isopropyl acetoacetate gave a (1:1) mixture of two tricyclic regioisomers (ISAM-M89A

and ISAM–M89B) that differ in the position (7/8) of the halogen atom. The unequivocal assignment for each regioisomer was determined by NMR techniques.

The binding data obtained from the five A_{2B} AR antagonists, the dual A_{2B} AR/ A_{2A} AR ligand and the A_{2A} AR clinical candidate (AZD-4635) are depicted in [figure 1B](#). The previously reported A_{2B} AR antagonists (SY1AF–30, SY1AF–80, SY1KO–24, ISAM–140) exhibit affinity values in the low nanomolar range ($K_i=3.50\text{--}24.3\text{ nM}$) and excellent subtype selectivity. Moreover, the diverse substitution pattern at the central pyrimidine scaffold provides chemical entities with different topologies, physicochemical features and distinctive binding modes, lately affecting its pharmacodynamic and pharmacokinetic profiles. ISAM–M89A and ISAM–R56A are novel non-xanthinic A_{2B} AR ligands discovered during the detailed exploration of the SAR around the tricyclic scaffold of ISAM–140 by halogen introduction and *N*-alkylation, respectively.

The selected A_{2B} AR and A_{2B} AR/ A_{2A} AR ligands were tested in cAMP assays ([figure 1B](#)) to evaluate their ability to inhibit NECA-stimulated (100 nM) cAMP production. These experiments demonstrated that all of them inhibited cAMP accumulation, thus validating its A_{2B} AR antagonistic behavior ([figure 1B](#)). A comparison of their K_i and K_b values revealed complete agreement (data within 1–7-fold) between the binding and functional assays. Ectonucleotidases, in particular CD73, play a key role in the context of adenosine-mediated tumor immune escape.⁴ Consequently, we evaluated the effect of A_{2B} AR ligands on the blockade of *h*CD73 as part of the pharmacological characterization of the selected A_{2B} AR ligands ([figure 1B](#)). These experiments revealed that none of the five A_{2B} AR antagonists, nor the A_{2A} / A_{2B} dual antagonist, showed any noticeable inhibitory effect on *h*CD73 (1 μM or 10 μM). These data excluded a dual A_{2B} AR-CD73 inhibition, allowing us to attribute the pharmacological effects described below to the specific A_{2B} AR antagonistic effect (or the dual A_{2A} / A_{2B} antagonism in the case of ISAM–M89A) of these ligands.

Binding mode of A_{2B} AR antagonists

The binding mode of the three most potent compounds (ISAM–140, ISAM–R56A and ISAM–M89A) was investigated using a previously reported A_{2B} AR homology model in complex with ISAM–140.³¹ Such a model could successfully explain the stereospecific recognition of trifluorinated derivatives ([figure 1C](#)), and the new antagonists ISAM–R56A and ISAM–M89A could indeed adopt an analogous binding mode within the orthosteric A_{2B} AR cavity ([figure 1C](#)). In all three cases, the tricyclic core is stabilized by interaction with the AR conserved residues N254^{6,55} and F173^{EL2}, a common denominator for AR ligands.³⁹ Ligand ISAM–M89A specifically maintained a double hydrogen bond with N254^{6,55}, allowing the chlorine atom in position eight to bind deeper in the binding pocket, surrounded by H251^{6,52}, N186^{5,42} and Q90^{3,37}. The N_1 substituted ISAM–R56A, which could only retain one hydrogen bond with N254^{6,55}, presented, on the other

hand, the extensive interactions of the 2-fluorobenzyl group in a A_{2B} AR specific hydrophobic pocket located between TM6 and TM7, formed by residues V253(I)^{6,54}, V250(L)^{6,51}, A271(L)^{7,34}, M272^{7,35}, A275^{7,38} and I276^{7,39} (parenthesis indicating the corresponding A_{2A} AR residues, if different). These specific interactions might explain the high affinity and the retained high selective profile for the A_{2B} AR.

Blockade of A_{2B} AR reduces patient-derived breast cancer spheroid growth

The expression of A_{2B} AR gene (*ADORA2B*) was investigated using *The Cancer Genome Atlas (TCGA)*—Pan cancer publicly available dataset across 33 tumor types (online supplemental figure 4A–D). With high *ADORA2B* gene expression in breast cancer, the blockade of the adenosinergic pathway has been widely studied in breast cancer.^{40–49} To investigate if our novel A_{2B} AR antagonists would affect breast cancer growth, we used a drug screening platform based on breast tumor resections.⁵⁰ It is composed of majority tumor cells at 73.2%, with 11.2% immune cells based on flow cytometry analysis of EpCAM and CD45 expression, respectively (online supplemental figure 4E,F). On exposure to ISAM–140, ISAM–R56A and ISAM–M89A for 4 days, the relative cell viability of these breast cancer spheroids was significantly reduced with a more pronounced effect by ISAM–M89A ([figure 2A](#)). To confirm this, antagonist effects of the cell growth, the kinetics of the observed cytotoxic effect mediated by the antagonists was studied using real-time imaging within the same spheroid culture setting ([figure 2B](#)). With the low and middle antagonist concentrations being statistically equal in cell viability, the latter concentration of ISAM–140, ISAM–R56A and ISAM–M89A significantly affected the spheroid growth over time compared with untreated control ([figure 2C](#)). Despite the low CD3 T cell frequency in these tumor resections (online supplemental figure 4F), blockade of A_{2B} AR still reduced cell viability and spheroid growth compared with untreated spheroids.

Blockade of A_{2B} AR rescues adenosine-mediated suppression of T and NK cell proliferation

To elucidate if the antitumor effects observed by the A_{2B} AR antagonists could alter lymphocyte activity, the different antagonists were added directly to T and NK cells in the presence of exogenous adenosine. While no statistical difference in viability at different adenosine concentrations was observed, a trend of decreasing viability with increasing adenosine concentration among CD8 T cell subsets was observed. Conversely, the viability of CD56 positive NK cells was not affected by adenosine (online supplemental figure 3B). However, a dose-dependent adenosine-mediated suppression of cell proliferation was observed across the different subtypes of T and NK cells with naïve CD8 T cells being the most affected (online supplemental figure 3C,D).

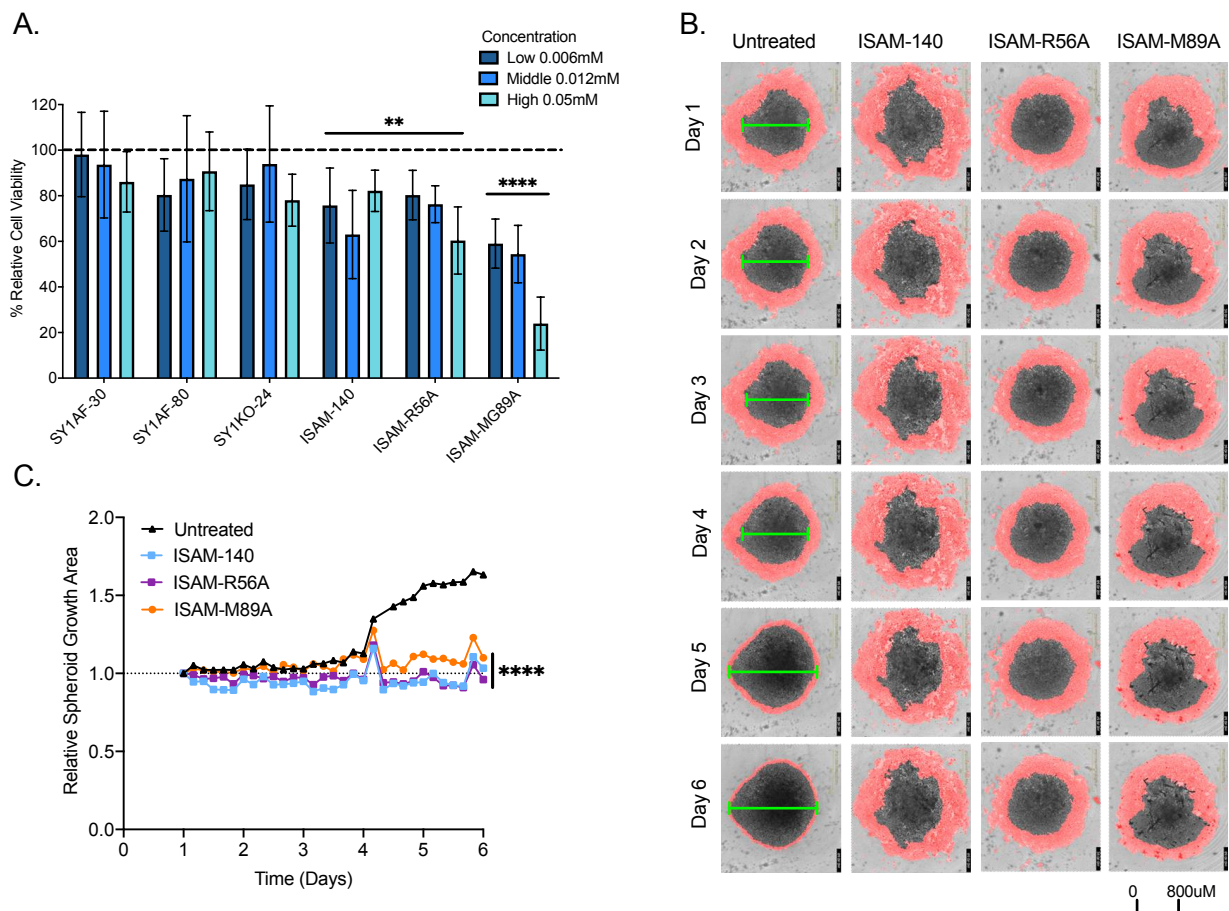


Figure 2 Antitumor effect of A_{2B} AR antagonists on breast cancer patient-derived spheroid cultures. (A) Relative cell viability to untreated antagonist control spheroid cultures ($n=3$, mean \pm SD) measured by Cell-Titer Glo assay. (B) Representative real time imaging of spheroid cultures over 6 days under 4X objective, with untreated (first column) or added 12 μ M concentration respective of A_{2B} AR antagonists indicated. Red mask demarcates area with cells surrounding the spheroid. Green line indicates estimated diameter of spheroid body. (C) Relative area of the representative spheroid growth (as shown in B) normalized to day 1. Statistical analysis—2-way (A) and 1-way (C) ANOVA with Dunnett’s multiple comparisons to untreated antagonist control was performed with * $p<0.05$, ** $p<0.01$, *** $p<0.001$, and **** $p<0.0001$.

Due to its suppressive effect on cell proliferation without compromising viability, adenosine concentration at 0.1 mM was used to investigate the ability of the different A_{2B} AR antagonists in rescuing adenosine-mediated suppression of lymphocyte proliferation. A subapoptotic concentration of 12 μ M A_{2B} AR antagonists was added to proliferating lymphocyte cultures (data not shown). ISAM-140 rescued the proliferation of CD45RA+ (naïve and effector) CD8 T cells, CD45RA- CD4T cells (central and effector memory) and CD45RA+ CD4T cells, and NK cells (figure 3). While ISAM-R56A did not restore the proliferation of T cell subsets, NK cell proliferation was significantly rescued. None of the other A_{2B} AR antagonists (SY1AF-30, SY1AF-80 and SY1KO-24) had any measurable impact on the rescue of lymphocyte proliferation (figure 3). Similarly, the dual A_{2A} AR/ A_{2B} AR antagonist ISAM-M89A or the A_{2A} AR antagonist AZD-4635 did not restore the proliferation of either T or NK cells.

Given the different effects on proliferation across lymphocyte subsets, we hypothesized that the expression of A_{2A} AR and A_{2B} AR might differ accordingly. Flow

cytometry analysis showed a highly donor-dependent variability of the expression intensity of A_{2A} AR and A_{2B} AR, and no significant difference in their expression was observed between the different lymphocyte populations (online supplemental figure 5). Similarly, the frequency of cells expressing A_{2A} AR and A_{2B} AR ranging between 10% and 20% did not differ between lymphocyte populations and was highly donor dependent (online supplemental figure 5E,F).

A_{2B} AR antagonists inhibit extracellular ADO by downregulating pAMPK in T cells with upregulation of expression of CD69, IFN γ , and perforin

To demonstrate the ability of A_{2B} AR antagonists to inhibit extracellular ADO uptake in lymphocytes, one of the downstream cellular ADO signaling molecules—phosphorylated-AMP activated protein kinase (pAMPK) was analyzed in total CD4 and CD8 T cells (figure 4A,B). ISAM-R56A significantly downregulated pAMPK among both CD4 and CD8 T cells in the presence of exogenous ADO.

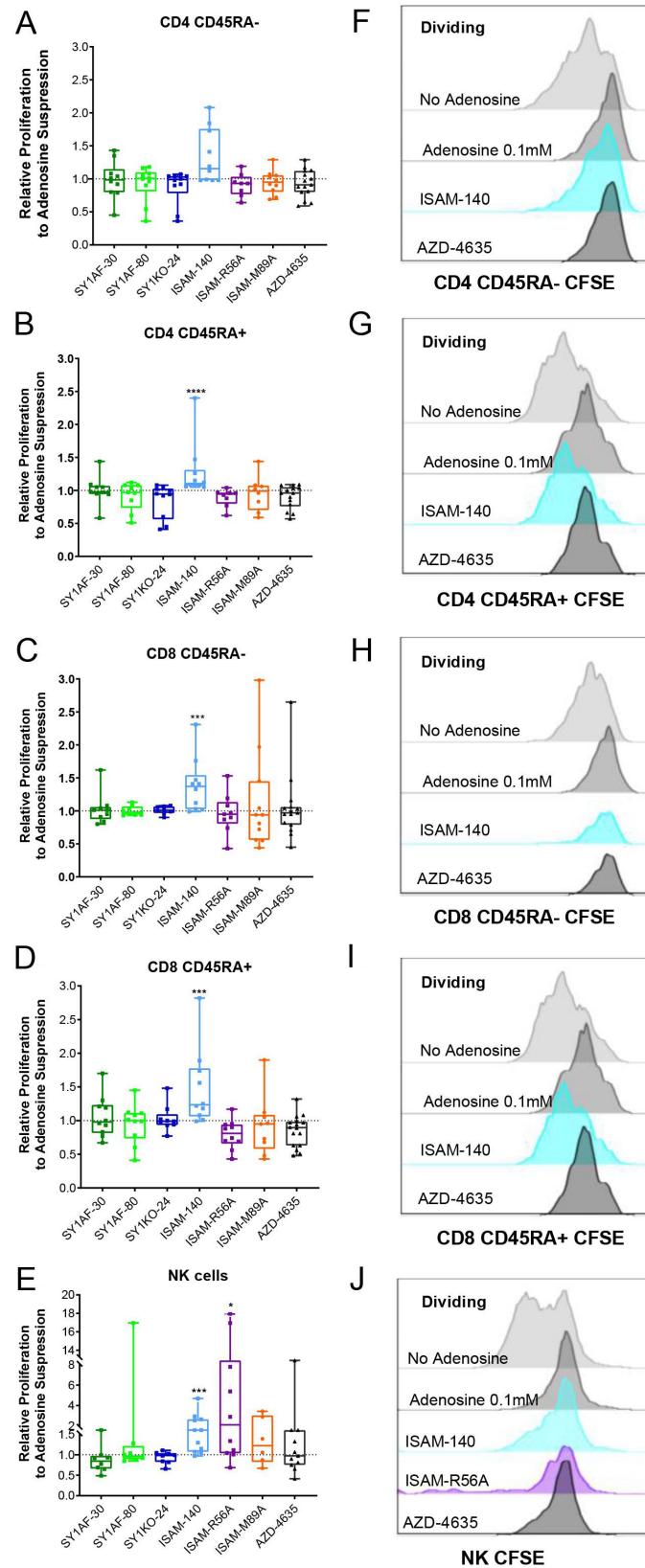


Figure 3 Rescue of lymphocyte proliferation by A_{2B} AR antagonism. Relative proliferation of: (A) CD45RA⁻ CD4 T cells, (B) CD45RA⁺ CD4 T cells, (C) CD45RA⁻ CD8 T cells, (D) CD45RA⁺ CD8 T cells, and (E) NK cells, after incubation with exogenous adenosine 0.1 mM and A_{2B} AR antagonist 12 μ M for 3 (A–D) and 6 (E) days. (n=10 healthy donors) CD45RA expression differentiates naïve and effector T cells from central and effector memory T cells. Box plots with minimum, first quartile, median, third quartile, and maximum are presented. Unpaired and non-parametric statistical analysis—Mann-Whitney test was performed against untreated control with * $p < 0.05$, ** $p < 0.01$, *** $p < 0.001$, and **** $p < 0.0001$. (F–J) Representative CFSE histogram on the corresponding lymphocyte subset. CFSE, carboxyfluorescein succinimidyl ester.

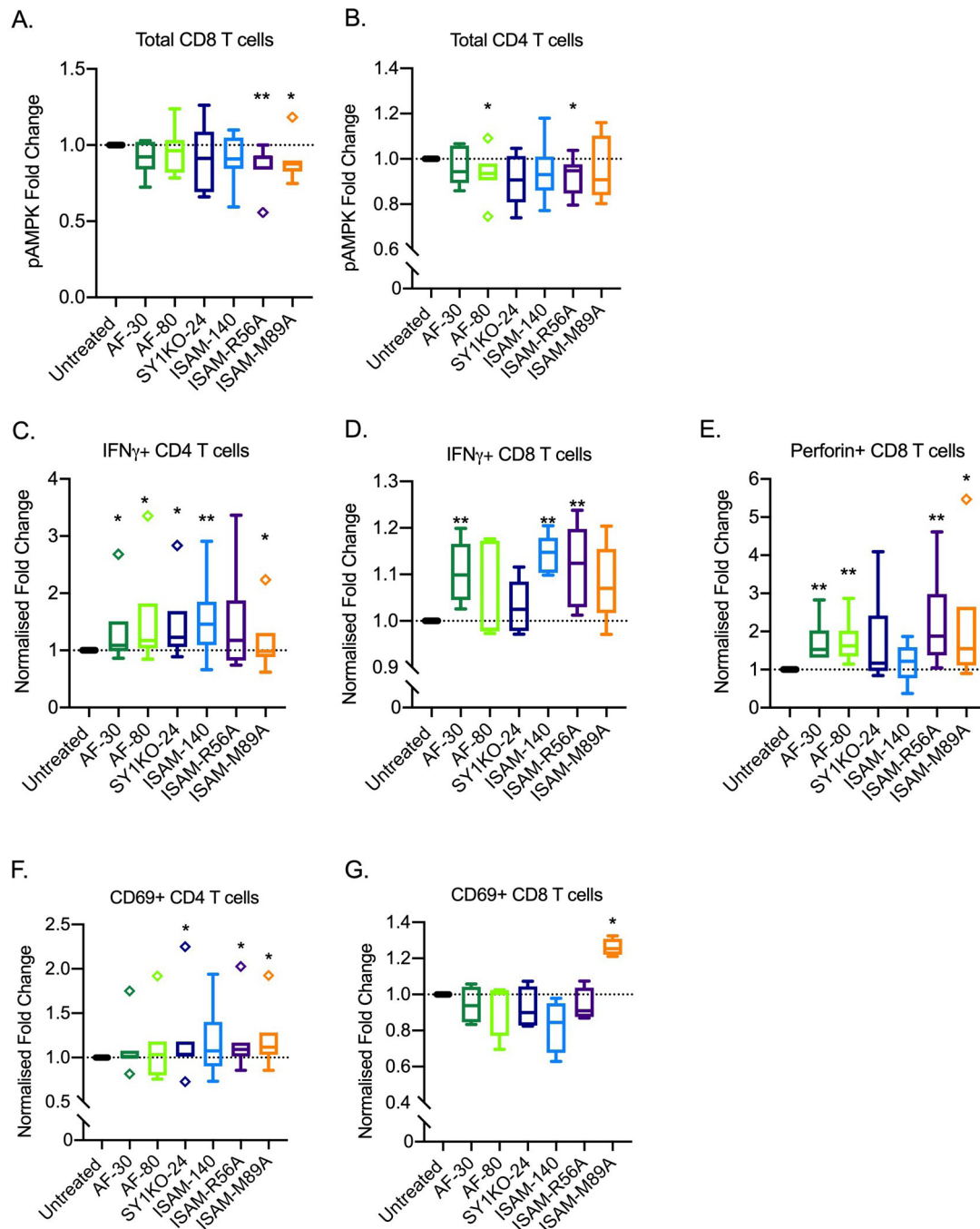


Figure 4 Rescue of lymphocyte proinflammatory cytokine production IFN γ and perforin by A_{2B} AR antagonism. (A,B) Inhibition of extracellular adenosine uptake via phosphorylated-AMP activated protein kinase (pAMPK) staining ($n=7$ healthy donors). Production of proinflammatory cytokines—(C,D) IFN γ and (E) perforin in CD4 ($n=5$ healthy donors) and CD8 ($n=6$ healthy donors) T cells. Expression of CD69 adhesion molecule in (F) CD4 ($n=7$ healthy donors) and (G) CD8 ($n=4$ healthy donors) T cells. A_{2B} AR antagonist $12\ \mu\text{M}$ was added. Outlier is presented as diamond shape and defined by Tukey's rule, which is not included in statistical analysis. Box plots with minimum, first quartile, median, third quartile, and maximum are presented. Normalized fold change is based on percent values compared with untreated controls. Unpaired and non-parametric statistical analysis—Mann-Whitney test was performed against untreated control with * $p<0.05$, ** $p<0.01$, *** $p<0.001$, and **** $p<0.0001$.

Similarly, SY1AF-80 and ISAM-M89A significantly inhibited ADO uptake in CD4 and CD8 T cells, respectively.

With the rescue of adenosine-mediated suppression of lymphocyte proliferation, effector function through proinflammatory cytokines—IFN γ and perforin, and the early activation marker—CD69 were successively

examined. IFN γ production by CD4 and CD8 T cells was successfully rescued by several antagonists (figure 4C,D). Similarly, perforin production by cytotoxic CD8 T cells was significantly upregulated on A_{2B} AR antagonisms (figure 4E), of which, SY1AF-30 and ISAM-R56A significantly improved both IFN γ and perforin production on

adenosine suppression. CD69 expression, associated with early lymphocyte activation, was also increased (figure 4F,G) whereby ISAM-M89A had positive effect on both CD4 and CD8 T cells. Finally, both ISAM-R56A and ISAM-M89A rescued killing of breast cancer TILs against autologous tumor cells while ISAM-R56A also rescued killing in sarcoma TILs (online supplemental figure 6).

A_{2B}AR antagonists rescue CD8 naïve T cell proliferation in adenosine-producing tumor spheroids

Sarcomas had the highest alteration frequencies for ADORA2B gene amplification as well as highest median copy number at DNA level when compared against 33 TCGA tumor types (online supplemental figure 4C,D). To investigate the effect of A_{2B}AR antagonism on lymphocyte proliferation in a more physiological relevant model, a sarcoma spheroid model that produce endogenous adenosine to better mimic the TME instead of using exogenous adenosine was developed. The relative production of adenosine was validated in spheroids including patient-derived tumors and the commercial U2OS cell line (online supplemental figure 7A). The expression of the ectonucleotidases CD39 and CD73 was highest in primary tumor spheroids from undifferentiated pleomorphic sarcoma, myxofibrosarcoma, and malignant peripheral nerve sheath tumors (MPNSTs, online supplemental figure 7B). Based on these results, lymphocyte proliferation was analyzed in MPNST-derived sarcoma spheroids. In contrast to the rescue of lymphocyte proliferation observed with exogenous adenosine, the A_{2B}AR antagonists SY1AF-30, SY1AF-80 and ISAM-R56A significantly rescued naïve and effector CD8 T cell proliferation based on CD45RA expression (figure 5).

A_{2B}AR antagonism improves TIL infiltration into autologous patient-derived sarcoma spheroids

To increase the translational impact of the immunomodulatory effects of the A_{2B}AR antagonists, their ability in rescuing adenosine-mediated suppression was tested in patient-derived ex vivo expanded tumor-infiltrating lymphocytes (TILs) and autologous sarcoma spheroids. These expanded TILs were mainly composed of CD4 and CD8 effector memory cells (online supplemental figure 7C-F). Real-time imaging showed the blockade of A_{2B}AR, especially by ISAM-R56A, resulted in an overall improved TIL infiltration in comparison with untreated tumor spheroids (figure 6A,B). Although not statistically significant, both ISAM-R89A and AZD-4635 treatments resulted in a median increased infiltration of 7% and 20%, respectively, whereas ISAM-140 did not have any effect on TIL infiltration (figure 6B). To confirm the frequency of TIL infiltration, the spheroids were collected and analyzed for CSFE positive and CD73 negative TILs by flow cytometry. Despite a high variability, ISAM-R56A treatment showed significantly enhanced TIL infiltration into the spheroids (figure 6C).

With the recruitment and retention of T cells within the tumor, expression of adhesion molecules is required.

Thus, the expression of tissue resident T cells markers-CD11a, CD49a, CD69 and CD103, was analyzed to gain insights into the phenotype of spheroid-infiltrated T cells. T-distributed stochastic neighboring embedding (tSNE) analysis revealed that the majority of infiltrating TILs are CD8 positive (cluster 1) and CD4 positive (cluster 9) T cells (figure 6D). Among them, the infiltrated CD8 T cells were enriched with 2.5-fold higher CD49a and CD103 coexpression, while no significant difference was observed, the infiltrated CD4 T cells showed an enrichment of CD69 (figure 6E-H). Furthermore, the total CD3 T cells were 20% greater inside the spheroid. To investigate the effect of A_{2B}AR antagonism in modulating the phenotype of infiltrated TILs, various antagonists were added to the TIL-tumor spheroids. All antagonists increased the CD8/CD4 T cell ratio though it was statistically significant only in the presence of ISAM-140 (figure 6I). In contrast, no significant change in the expression of the adhesion molecules CD11a, CD69, and CD49a/CD103 between untreated and A_{2B}AR antagonist-treated spheroid cultures was observed (figure 6J-L, online supplemental figure 8).

DISCUSSION

While blockade of A_{2A}AR is well documented to rescue T and NK cell proliferation, the effect of targeting the A_{2B}AR in lymphocytes remains almost unexplored.^{8 13 16} Only recently, it was reported that A_{2B}AR deficiency in tumor-bearing mice resulted in an increased infiltration of dendritic cells to promote cross-priming of adoptively transferred tumor antigen-specific T cells.²¹ A_{2B}AR activation plays critical roles during tumor development including but not limited to proliferation, angiogenesis, invasion and metastasis, as well as immune suppression, which make the antagonists of this receptor hold great promise for the development of new polyvalent cancer therapeutics.^{5 6} To investigate lymphocyte activity on blockade of A_{2B}AR, a set of five potent and selective A_{2B}AR antagonists and a dual A_{2A}AR/A_{2B}AR antagonist were synthesized and evaluated. Herein, documented ligands were conceived in the context of a hit to lead program based on the 1,4-dihydrobenzo⁴⁵imidazo[1,2-a]pyrimidine scaffold. The obtained data highlight the potential of this scaffold to provide potent AR antagonists while illustrating how subtle structural modifications can strongly affect the affinity and selectivity profile of the novel ligands. The main SAR and selectivity trends identified within the series were substantiated by a molecular modeling study based on a receptor-driven docking model of A_{2B}AR constructed based on the crystal structure specific of the human A_{2A}AR.

Given the short half-life of endogenous adenosine,⁴⁷ exogenous adenosine is still commonly used to study adenosine-mediated immunosuppression in the TME. In general, lymphocyte assays are based on phenotypic analysis and often complemented with read-outs to analyze canonical functions such as cell viability, proliferation and the ability to produce inflammatory cytokines as well

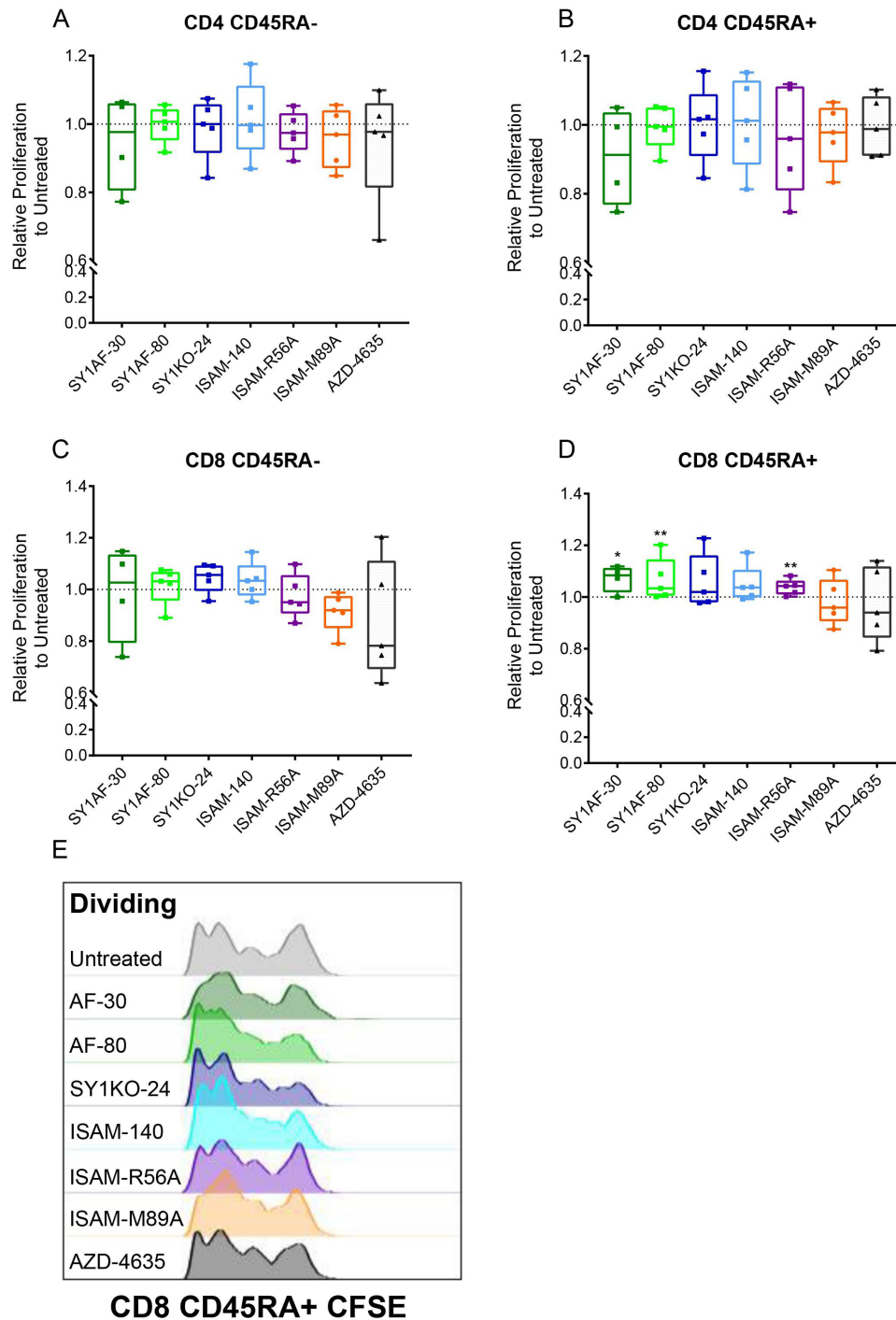


Figure 5 Rescue of lymphocyte proliferation in sarcoma spheroids by A_{2B} AR antagonism. Relative proliferation of: (A) CD45RA-CD4 T cells, (B) CD45RA+CD4 T cells, (C) CD45RA- CD8 T cells and (D) CD45RA+ CD8 T cells after antagonist $12\ \mu\text{M}$ treatment for 3 days in MPNST patient-derived sarcoma spheroid. ($n=5$ healthy donors) Box plots with minimum, first quartile, median, third quartile, and maximum are presented. Unpaired and non-parametric statistical analysis—Mann-Whitney test was performed against untreated control with * $p<0.05$, ** $p<0.01$, *** $p<0.001$, and **** $p<0.0001$. (E) Representative CFSE dilution of CD45RA+ CD8 T cells. CD45RA expression differentiates naïve and effector T cells from central and effector memory T cells. MPNST, malignant peripheral nerve sheath tumors; UPS, undifferentiated pleomorphic sarcoma.

as to recognize and kill target cells. Throughout these experiments, the A_{2B} AR antagonists were evaluated in lymphocyte viability and proliferation assays. Since prognosis is often associated with the frequency of TILs,^{51–53} we developed two models to study the blockage of A_{2B} AR in recusing antitumor immune responses. An exogenous

adenosine in vitro healthy donor model and endogenously produced adenosine ex vivo patient-derived model were used to better study the dynamic crosstalk of adenosine in the TME as well as being clinically relevance. As a result, A_{2B} AR antagonists successfully rescued antitumor immune response through cytotoxicity of patient-derived

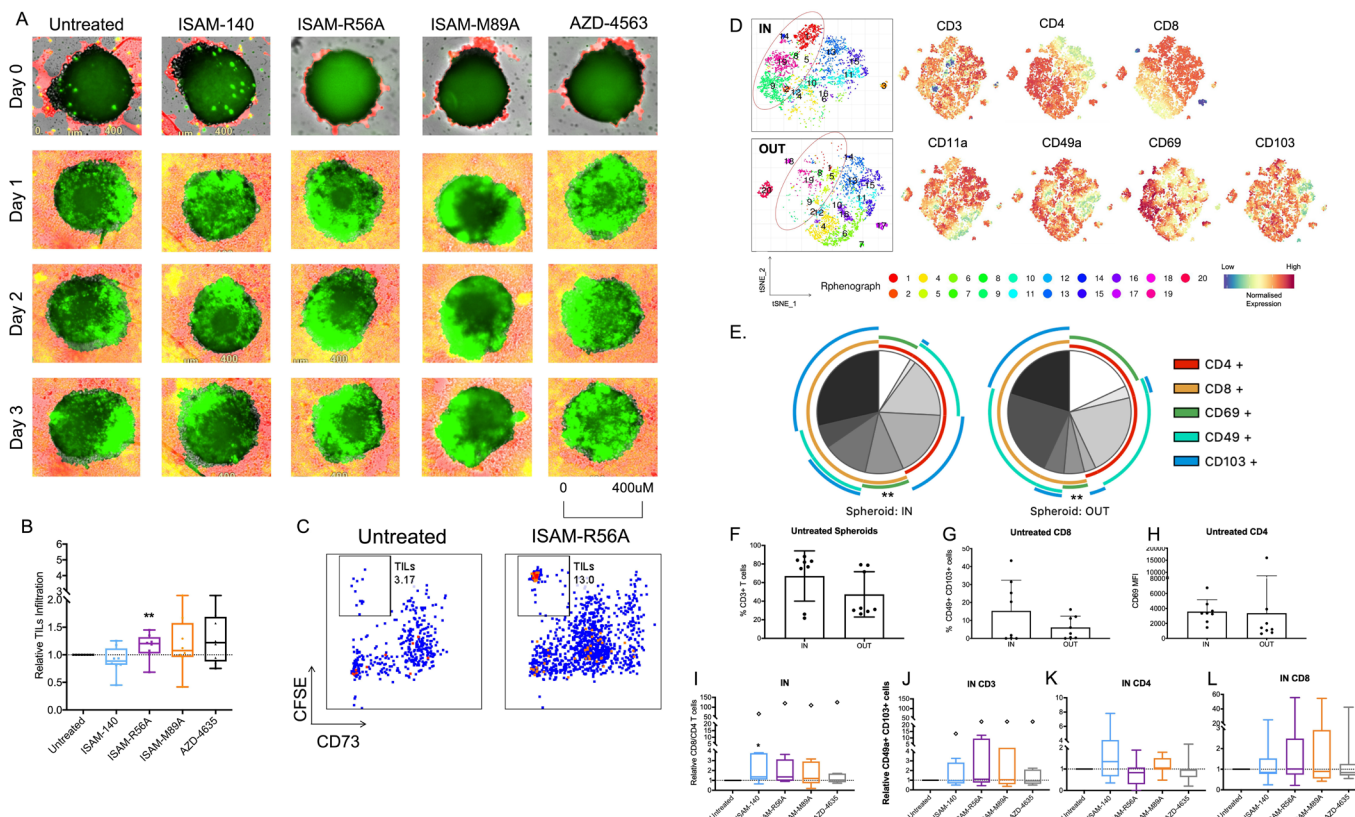


Figure 6 Infiltration of TILs into autologous patient-derived sarcoma spheroids after A_{2B} AR antagonist treatment. (A) Representative real-time imaging of spheroid TIL infiltration over 3 days under 4 \times objective. Green areas demarcate CFSE-labeled TILs infiltrated into the red boundary tumor spheroid. (B) Relative TIL infiltration into autologous spheroids (n=8 donors) measured by flow cytometer. Antagonist 12 μ M was added with CFSE-labeled TILs after spheroid formation on day five. (C) Representative flow cytometry plot of CFSE positive TILs in CD73+ tumor spheroid. (D) tSNE analysis and (E) annotated pie chart of TILs within (IN) and outside of (OUT) the spheroids without treatment (n=8 donors, indicated within the pie chart). Wilcoxon Rank Sum test was performed to compare the various IN vs OUT adhesion markers. Expression of (F) CD3 T cells, (G) CD49a+ CD103+ among CD8 T cells and (H) CD69 MFI among CD4 T cells IN and OUT of the spheroids without treatment (n=8 donors). (I) Relative CD8/CD4 TIL ratio IN the spheroids. Differential expression of relative (J–L). CD49a+ CD103+ cells IN the spheroids (n=8 donors) of CD3, CD8, and CD4 TILs. Antagonist 12 μ M was added for J–L. Outlier is presented as diamond shape and defined by Tukey’s rule, which is not included in statistical analysis. Box plots with minimum, first quartile, median, third quartile, and maximum are presented. Unpaired and non-parametric statistical analysis—Mann-Whitney test was performed against untreated control with * p <0.05, ** p <0.01, *** p <0.001, and **** p <0.0001. CFSE, carboxyfluorescein succinimidyl ester; TIL, tumor infiltrating lymphocyte; tSNE, T-distributed stochastic neighboring embedding.

spheroid cultures, proliferation of lymphocytes and tumor spheroid immune cell infiltration accompanied with differences in phenotype.

The six ligands examined exhibited high A_{2B} AR affinity and excellent selectivity profiles. Two of them (ISAM–R56A and ISAM–M89A) were herein originally reported, by introduction of a 2-fluorobenzyl group or a chlorine atom at positions 1 and 8 of the tricyclic core, respectively. Indeed, ISAM–R56A (Ki=1.50 nM) is confirmed as one of the most potent A_{2B} AR antagonist published to date, while ISAM–M89A exhibited a highly promising dual A_{2B} AR/ A_{2A} AR antagonistic profile (while devoid of affinity for the remaining AR subtypes). The selected ligands revealed negligible CD73 inhibitory action, thus allowing to attribute the herein observed effects to their specific A_{2B} AR antagonistic effect. The high affinity of these compounds could be explained by a computational model of the

A_{2B} AR in complex with these ligand chemotype, which had been used in the design of these series of antagonists.

By exposure of these A_{2B} AR antagonists to breast cancer patient-derived cells, their antitumor activity was first revealed through a reduced tumor spheroids growth rate. Despite the highly variable donor-dependent expression of A_{2B} ARs, the immunomodulatory effect of A_{2B} AR antagonism was further demonstrated with the successful rescue of T and NK cell proliferation under exogenous adenosine-mediated suppression, with CD8 naïve T cell being the most responsive of the T cell types examined. These findings correspond to an adenosine-producing human melanoma cell line, showing higher suppression of CD8 T cell proliferation than CD4 T cells.⁵⁴ A_{2B} AR antagonists were subsequently shown to inhibit extracellular ADO uptake via downstream pAMPK in total CD4 and CD8 T cells. Even with varying adenosine

susceptibility between donors, improved production of proinflammatory cytokines IFN γ and perforin along with the expression of the activation marker CD69 was observed. In addition, the obtained discrepancies could be related with drug availability, binding kinetics and physicochemical properties, influencing a different cell response for drugs with similar affinity.

Patient outcome in various sarcoma types is shown to correlate with the presence of TILs.^{52–53–55} Patient-derived spheroids can retain the unique characteristic of the original tumor compared with 2D monoculture or patient-derived xenograft by enabling cell-cell and cell-extracellular interactions.^{56–57} Using a patient-derived sarcoma spheroids model, we observed that treatment with A_{2B}AR antagonists improved autologous TIL infiltration into sarcoma spheroids. Tumor spheroid-infiltrating lymphocytes were enriched for the expression of the tissue resident markers CD49a and CD103 in CD8 T cells and CD69 in CD4 T cells.⁵⁸ A recent study identified a unique population of CD8 TILs coexpressing CD39 and CD103 that were reactive against both primary and metastatic tumors.⁵⁹ Another study defined CD8 tissue resident T cells in human epithelia with cytotoxic function to express CD49a and correlate with inflammatory skin diseases.⁶⁰ In vivo A_{2A}AR antagonism has also been reported to upregulate the expression of CD69 on TILs, while A_{2B}AR antagonism enhanced CXCR3-dependent TIL responses.^{61–62} Notably, a recent study demonstrated that adenosine can mediate functional and metabolic suppression of tumor-infiltrating CD8+ T cells.³⁷ Thereby, A_{2B}AR antagonism not only potentially increase TIL infiltration into solid tumors through modulation of adhesion molecules but may also improve the overall metabolic fitness of tumor-infiltrating T cells.

ISAM-140, a potent and highly selective A_{2B}AR antagonist ($K_i=3.49$ nM), was shown as an optimal A_{2B}AR binder by computational modeling and proved to be an efficient antagonist in functional cAMP assay.³⁰ We here demonstrate that this compound exerts biologically improved immune cell proliferation on T and NK cells in an A_{2B}AR expression independent manner in healthy donor PBMCs. This response was dose-dependent with a higher concentration further restoring proliferation (data not shown). This lymphocyte proliferation rescue was accompanied with upregulated IFN γ production in both CD4 and CD8 T cells. ISAM-140 was also non-toxic and even improved cell viability (data not shown). In addition, a novel A_{2B}AR antagonist—ISAM-R56A, with K_i to the A_{2B}AR similar to the corresponding A_{2A}AR value of the preclinical A_{2A}AR antagonist—AZD-4635 (1.50 nM vs 1.70 nM, respectively), improved TILs infiltration into autologous patient-derived sarcoma spheroids. CD8-naïve T-cell proliferation response was also observed in the adenosine-producing spheroid model, while a specific NK cell proliferation response was noted in the exogenous adenosine assay. CD8 T cell IFN γ and perforin production was also significantly rescued under exogenous adenosine suppression. Thereby, the potential

of ISAM-R56A to induce tumorous TILs infiltration is highly promising. This induction of tumorous CD8 T cell infiltration was already observed from the clinical trial of a dual A_{2A}AR/A_{2B}AR antagonist—AB928 combined treatment with anti-PD1.⁶³

CONCLUSION

With only one A_{2B}AR antagonist currently registered in a clinical trial,³ our findings close the gap of lacking alternatives and provide insights to practical readouts related to adenosine-mediated immune suppression. We established a systematic workflow to screen novel small molecule antagonists that enabled the identification of ISAM-R56A as the most potent candidate for A_{2B}AR blockade. With ISAM-R56A, cytotoxic immune cells can be relieved from adenosine-mediated suppression to proliferate and infiltrate into adenosine-producing solid tumors expressing CD73. Besides using appropriate immunocompetent or xenograft in vivo models to evaluate the pharmacology and preclinical safety of these novel small molecule antagonists as potential complements to existing immunotherapies, future directions on downstream hypoxia-HIF-1 α of A₂AR-cAMP signaling axis shall be mimicked in in vitro and ex vivo assays.

Author affiliations

- ¹Department of Biological Science, Nanyang Technological University, Singapore
- ²Department of Oncology-Pathology, Karolinska Institute, Stockholm, Sweden
- ³Center for Research in Biological Chemistry and Molecular Materials, University of Santiago de Compostela, Santiago de Compostela, Galicia, Spain
- ⁴Singapore Immunology Network SigN, Agency for Science, Technology and Research, Singapore, Republic of Singapore
- ⁵Department of Microbiology Tumor and Cell Biology, Karolinska Institutet, Stockholm, Sweden
- ⁶Department of Applied Physics, Science for Life Laboratory, KTH Royal Institute of Technology, Stockholm, Sweden
- ⁷Department of Clinical Pathology and Cancer Diagnostics, Karolinska University Hospital, Stockholm, Sweden
- ⁸Center for Research in Molecular Medicine and Chronic Diseases, University of Santiago de Compostela, Santiago de Compostela, Galicia, Spain
- ⁹Department of Cell and Molecular Biology, Uppsala University, Uppsala, Sweden
- ¹⁰Department of Cell and Molecular Biology, Science for Life Laboratory, Uppsala University, Uppsala, Sweden

Correction notice This article has been corrected since it was first published online. The x-axis on figures 4B, D, F and G has been updated.

Twitter Rubén Prieto-Díaz @bentoaz and Hugo Gutierrez-de-Teran @hugogdtc

Acknowledgements Support from the Swedish strategic research program eSENCE, the Swedish Cancer Society (#CAN 2018/451), and The Cancer Research Fundations of Radiumhemmet (#181183) is acknowledged. The computations were performed on resources provided by the Swedish National Infrastructure for Computing (SNIC). This research program has been developed in the frame of the European COST action ERNEST (CA 18133).

Contributors AL and ES conceived, designed, and supervised the study and acted as guarantors. RP-D, MM, JA and XG-M participated in the synthesis and characterization of the ligands. AHMT, SN, LT, XC and JH performed the cellular and immunological studies. JMB and MIL evaluated the binding affinity and CD73 activity. HG-d-T and WJ performed the computational assays. AHMT, RP-D, AL, and ES analyzed the data and written the manuscript. All authors have given approval to the final version of the manuscript.

Funding This work was financially supported by the Consellería de Cultura, Educación e Ordenación Universitaria of the Galician Government: (grant:

ED431B2017/70), Centro singular de Investigación de Galicia accreditation 2019-2022 (ED431G 2019/03), and the European Regional Development Fund (ERDF), the Swedish Research Council.

Competing interests None declared

Patient consent for publication Not applicable.

Ethics approval Buffy coat and plasma from anonymized adult healthy blood donors was obtained from Karolinska University Hospital Blood Bank. For surgical resections of sarcoma and breast tumors, ethical approval (#2013/1979-31, #2016/957-31, #2017/742-32) from Karolinska Institutet Ethical Review Board and patient's informed consent were obtained in accordance with the Declaration of Helsinki.

Provenance and peer review Not commissioned; externally peer reviewed.

Data availability statement Data are available on reasonable request.

Supplemental material This content has been supplied by the author(s). It has not been vetted by BMJ Publishing Group Limited (BMJ) and may not have been peer-reviewed. Any opinions or recommendations discussed are solely those of the author(s) and are not endorsed by BMJ. BMJ disclaims all liability and responsibility arising from any reliance placed on the content. Where the content includes any translated material, BMJ does not warrant the accuracy and reliability of the translations (including but not limited to local regulations, clinical guidelines, terminology, drug names and drug dosages), and is not responsible for any error and/or omissions arising from translation and adaptation or otherwise.

Open access This is an open access article distributed in accordance with the Creative Commons Attribution 4.0 Unported (CC BY 4.0) license, which permits others to copy, redistribute, remix, transform and build upon this work for any purpose, provided the original work is properly cited, a link to the licence is given, and indication of whether changes were made. See <https://creativecommons.org/licenses/by/4.0/>.

ORCID iDs

Apple Hui Min Tay <http://orcid.org/0000-0002-0600-6599>

Xinsong Chen <http://orcid.org/0000-0002-3214-9075>

Hugo Gutierrez-de-Teran <http://orcid.org/0000-0003-0459-3491>

Andreas Lundqvist <http://orcid.org/0000-0002-9709-2970>

REFERENCES

- Hanahan D, Weinberg RA. Hallmarks of cancer: the next generation. *Cell* 2011;144:646–74.
- Marshall HT, Djarnoz MBA. Immuno-oncology: emerging targets and combination therapies. *Front Oncol* 2018;8:315.
- Li X, Wenes M, Romero P, et al. Navigating metabolic pathways to enhance antitumor immunity and immunotherapy. *Nat Rev Clin Oncol* 2019;16:425–41.
- Vijayan D, Young A, Teng MWL, et al. Targeting immunosuppressive adenosine in cancer. *Nat Rev Cancer* 2017;17:709–24.
- Gao Z-G, Jacobson KA. A2B adenosine receptor and cancer. *Int J Mol Sci* 2019;20:5139–18.
- Di Virgilio F, Adinolfi E. Extracellular purines, purinergic receptors and tumor growth. *Oncogene* 2017;36:293–303.
- Kumar V. Adenosine as an endogenous immunoregulator in cancer pathogenesis: where to go? *Purinergic Signal* 2013;9:145–65.
- Ohta A, Gorelik E, Prasad SJ, et al. A2A adenosine receptor protects tumors from antitumor T cells. *Proc Natl Acad Sci U S A* 2006;103:13132–7.
- Ballarin M, Fredholm BB, Ambrosio S, et al. Extracellular levels of adenosine and its metabolites in the striatum of awake rats: inhibition of uptake and metabolism. *Acta Physiol Scand* 1991;142:97–103.
- Miller WL, Thomas RA, Berne RM, et al. Adenosine production in the ischemic kidney. *Circ Res* 1978;43:390–7.
- Ohta A, Sitkovsky M. Role of G-protein-coupled adenosine receptors in downregulation of inflammation and protection from tissue damage. *Nature* 2001;414:916–20.
- Cekic C, Linden J. Adenosine A2A receptors intrinsically regulate CD8+ T cells in the tumor microenvironment. *Cancer Res* 2014;74:7239–49.
- Kjaergaard J, Hatfield S, Jones G. A_{2A} adenosine receptor gene deletion or synthetic A_{2A} antagonist liberate tumor-reactive CD8+ T cells from tumor-induced immunosuppression. *Ji* 2018;201:782–91.
- Ohta A, Kini R, Ohta A, et al. The development and immunosuppressive functions of CD4+ CD25+ Foxp3+ regulatory T cells are under influence of the adenosine-A2A adenosine receptor pathway. *Front Immunol* 2012;3:1–12.
- Panther E, Corinti S, Idzko M, et al. Adenosine affects expression of membrane molecules, cytokine and chemokine release, and the T-cell stimulatory capacity of human dendritic cells. *Blood* 2003;101:3985–90.
- Sitkovsky MV. Lessons from the A2A adenosine receptor antagonist-enabled tumor regression and survival in patients with treatment-refractory renal cell cancer. *Cancer Discov* 2020;10:16–19.
- Borodovsky A, Barbon CM, Wang Y, et al. Small molecule AZD4635 inhibitor of A_{2A}R signaling rescues immune cell function including CD103+ dendritic cells enhancing anti-tumor immunity. *J Immunother Cancer* 2020;8:1–17.
- Congreve M, Brown GA, Borodovsky A, et al. Targeting adenosine A_{2A} receptor antagonism for treatment of cancer. *Expert Opin Drug Discov* 2018;13:997–1003.
- Hinz S, Navarro G, Borroto-Escuela D, et al. Adenosine A_{2A} receptor ligand recognition and signaling is blocked by A_{2B} receptors. *Oncotarget* 2018;9:24423 doi:10.18632/oncotarget.24423
- Maj T, Wang W, Crespo J, et al. Oxidative stress controls regulatory T cell apoptosis and suppressor activity and PD-L1-blockade resistance in tumor. *Nat Immunol* 2017;18:1332.
- Chen S, Akdemir I, Fan J, et al. The expression of adenosine A2B receptor on antigen-presenting cells suppresses CD8+ T-cell responses and promotes tumor growth. *Cancer Immunol Res* 2020;8:canimm.0833.2019.
- Corona SP, Sobhani N, Generali D. Adenosine A2B receptor: novel anti-cancer therapeutic implications. *J Cancer Metastasis Treat* 2017;3:206.
- Antonoli L, Blandizzi C, Pacher P, et al. Immunity, inflammation and cancer: a leading role for adenosine. *Nat Rev Cancer* 2013;13:842–57.
- Leone RD, Emens LA. Targeting adenosine for cancer immunotherapy. *J Immunother Cancer* 2018;6:1–9.
- Moriyama K, Sitkovsky MV. Adenosine A2A receptor is involved in cell surface expression of A2B receptor. *J Biol Chem* 2010;285:39271–88.
- Mallo-Abreu A, Prieto-Díaz R, Jespers W, et al. Nitrogen-Walk approach to explore bioisosteric replacements in a series of potent A_{2B} receptor antagonists. *J Med Chem* 2020;63:7721–39.
- Jiang J, Seel CJ, Temirak A, et al. A_{2B} adenosine receptor antagonists with picomolar potency. *J Med Chem* 2019;62:4032–55.
- Carbajales C, Azuaje J, Oliveira A, et al. Enantiospecific Recognition at the A_{2B} Adenosine Receptor by Alkyl 2-Cyanoimino-4-substituted-6-methyl-1,2,3,4-tetrahydropyrimidine-5-carboxylates. *J Med Chem* 2017;60:3372–82.
- Crespo A, El Maatougui A, Biagini P. Discovery of 3,4-dihydropyrimidin-2(1H)-ones as a novel class of potent and selective A2B 2B adenosine receptor antagonists. *ACS Med Chem Lett* 2013;4:1031–6.
- El Maatougui A, Azuaje J, González-Gómez M, et al. Discovery of potent and highly selective A2B adenosine receptor antagonist chemotypes. *J Med Chem* 2016;59:1967–83.
- Mallo-Abreu A, Majellaro M, Jespers W, et al. Trifluorinated pyrimidine-based A_{2B} antagonists: optimization and evidence of stereospecific recognition. *J Med Chem* 2019;62:9315–30.
- Jaakola V-P, Griffith MT, Hanson MA, et al. The 2.6 angstrom crystal structure of a human A2A adenosine receptor bound to an antagonist. *Science* 2008;322:1211–7.
- Esguerra M, Siretskiy A, Bello X, et al. GPCR-ModSim: a comprehensive web based solution for modeling G-protein coupled receptors. *Nucleic Acids Res* 2016;44:W455–62.
- Bauer P, Barrozo A, Purg M, et al. Q6: a comprehensive toolkit for empirical valence bond and related free energy calculations. *SoftwareX* 2018;7:388–95.
- Schrödinger. *Schrödinger*. LLC New York, 2009.
- Yang Y, Neo SY, Chen Z, et al. Thioredoxin activity confers resistance against oxidative stress in tumor-infiltrating NK cells. *J Clin Invest* 2020;130:5508–22.
- Mastelic-Gavillet B, Navarro Rodrigo B, Décombaz L, et al. Adenosine mediates functional and metabolic suppression of peripheral and tumor-infiltrating CD8+ T cells. *J Immunother Cancer* 2019;7:1–16.
- Kappe CO. Biologically active dihydropyrimidones of the Biginelli-type—a literature survey. *Eur J Med Chem* 2000;35:1043–52.
- Jespers W, Schiedel AC, Heitman LH, et al. Structural mapping of adenosine receptor mutations: ligand binding and signaling mechanisms. *Trends Pharmacol Sci* 2018;39:75–89.
- Gil Del Alcazar CR, Huh SJ, Ekram MB, et al. Immune escape in breast cancer during *In Situ* to invasive carcinoma transition. *Cancer Discov* 2017;7:1098–115.

- 41 Gourdin N, Bossennec M, Rodriguez C, *et al.* Autocrine adenosine regulates tumor polyfunctional CD73⁺CD4⁺ effector T cells devoid of immune checkpoints. *Cancer Res* 2018;78:3604–18.
- 42 Loi S, Pommey S, Haibe-Kains B, *et al.* CD73 promotes anthracycline resistance and poor prognosis in triple negative breast cancer. *Proc Natl Acad Sci U S A* 2013;110:11091–6.
- 43 Mittal D, Sinha D, Barkauskas D, *et al.* Adenosine 2B receptor expression on cancer cells promotes metastasis. *Cancer Res* 2016;76:4372–82.
- 44 Stagg J, Divisekera U, McLaughlin N, *et al.* Anti-CD73 antibody therapy inhibits breast tumor growth and metastasis. *Proc Natl Acad Sci U S A* 2010;107:1547–52.
- 45 Terp MG, Olesen KA, Arnspang EC, *et al.* Anti-human CD73 monoclonal antibody inhibits metastasis formation in human breast cancer by inducing clustering and internalization of CD73 expressed on the surface of cancer cells. *J Immunol* 2013;191:4165–73.
- 46 Turcotte M, Allard D, Mittal D, *et al.* CD73 promotes resistance to HER2/ErbB2 antibody therapy. *Cancer Res* 2017;77:5652–63.
- 47 Zhi X, Chen S, Zhou P, *et al.* RNA interference of ecto-5'-nucleotidase (CD73) inhibits human breast cancer cell growth and invasion. *Clin Exp Metastasis* 2007;24:439–48.
- 48 Zhou X, Zhi X, Zhou P, *et al.* Effects of ecto-5'-nucleotidase on human breast cancer cell growth in vitro and in vivo. *Oncol Rep* 2007;17:1341–6.
- 49 Sepúlveda C, Palomo I, Fuentes E. Role of adenosine A2B receptor overexpression in tumor progression. *Life Sci* 2016;166:92–9.
- 50 Sekhon BK, Roubin RH, Tan A, *et al.* High-throughput screening platform for anticancer therapeutic drug cytotoxicity. *Assay Drug Dev Technol* 2008;6:711–21.
- 51 Rusakiewicz S, Semeraro M, Sarabi M, *et al.* Immune infiltrates are prognostic factors in localized gastrointestinal stromal tumors. *Cancer Res* 2013;73:3499–510.
- 52 Fujii H, Arakawa A, Utsumi D, *et al.* CD8(+) tumor-infiltrating lymphocytes at primary sites as a possible prognostic factor of cutaneous angiosarcoma. *Int J Cancer* 2014;134:2393–402.
- 53 Balch CM, Riley LB, Bae YJ, *et al.* Patterns of human tumor-infiltrating lymphocytes in 120 human cancers. *Arch Surg* 1990;125:200–5.
- 54 Morandi F, Morandi B, Horenstein AL, *et al.* A non-canonical adenosinergic pathway led by CD38 in human melanoma cells induces suppression of T cell proliferation. *Oncotarget* 2015;6:25602–18.
- 55 Rusakiewicz S, Semeraro M, Sarabi M, *et al.* Immune infiltrates are prognostic factors in localized gastrointestinal stromal tumors. *Cancer Res* 2013;73:3499–510.
- 56 Bray LJ, Huttmacher DW, Bock N. Addressing patient specificity in the engineering of tumor models. *Front Bioeng Biotechnol* 2019;7:217.
- 57 Liao W, Wang J, Xu J, *et al.* High-throughput three-dimensional spheroid tumor model using a novel stamp-like tool. *J Tissue Eng* 2019;10:2041731419889184.
- 58 Amsen D, van Gisbergen KPJM, Hombrink P, *et al.* Tissue-resident memory T cells at the center of immunity to solid tumors. *Nat Immunol* 2018;19:538–46.
- 59 Duhon T, Duhon R, Montler R, *et al.* Co-expression of CD39 and CD103 identifies tumor-reactive CD8 T cells in human solid tumors. *Nat Commun* 2018;9:2724.
- 60 Cheuk S, Schlums H, Gallais Sérézal I, *et al.* CD49a Expression Defines Tissue-Resident CD8⁺ T Cells Poised for Cytotoxic Function in Human Skin. *Immunity* 2017;46:287–300.
- 61 Leone RD, Sun I-M, Oh M-H, *et al.* Inhibition of the adenosine A2A receptor modulates expression of T cell coinhibitory receptors and improves effector function for enhanced checkpoint blockade and act in murine cancer models. *Cancer Immunol Immunother* 2018;67:1271–84.
- 62 Young A, Ngiew SF, Madore J, *et al.* Targeting adenosine in BRAF-mutant melanoma reduces tumor growth and metastasis. *Cancer Res* 2017;77:4684–96.
- 63 Powderly JD, de Souza PL, Gutierrez R, *et al.* AB928, a novel dual adenosine receptor antagonist, combined with chemotherapy or AB122 (anti-PD-1) in patients (PTS) with advanced tumors: preliminary results from ongoing phase I studies. *JCO* 2019;37:2604.

Correction: A2B adenosine receptor antagonists rescue lymphocyte activity in adenosine-producing patient-derived cancer models

Tay AHM, Prieto-Díaz R, Neo S, et al. A2B adenosine receptor antagonists rescue lymphocyte activity in adenosine-producing patient-derived cancer models. *J Immunother Cancer* 2022; **10**: e004592. doi: 10.1136/jitc-2022-004592.

In this article The x-axis on figures 4B, D, F and G have been updated to include the correct values.

Open access This is an open access article distributed in accordance with the Creative Commons Attribution 4.0 Unported (CC BY 4.0) license, which permits others to copy, redistribute, remix, transform and build upon this work for any purpose, provided the original work is properly cited, a link to the licence is given, and indication of whether changes were made. See <https://creativecommons.org/licenses/by/4.0/>.

© Author(s) (or their employer(s)) 2023. Re-use permitted under CC BY. Published by BMJ.

J Immunother Cancer 2024;**12**:e004592corr1. doi:10.1136/jitc-2022-004592corr1



SUPPORTING INFORMATION

A_{2B} Adenosine Receptor Antagonists Rescue Lymphocyte Activity in Adenosine-Producing Patient-Derived Cancer Models

Apple Tay Hui Min,^{1,2,‡} Rubén Prieto-Díaz,^{3,‡} Shiyong Neo,^{1,4} Le Tong,¹ Xinsong Chen,¹ Valentina,⁵ Björn Önfelt,^{5,6} Johan Hartman,¹ Felix Haglund,¹ Maria Majellaro,³ Jhonny Azuaje,³ Xerardo Garcia-Mera,³ Jose M. Brea,⁶ Maria I. Loza,⁶ Willem Jaspers,⁸ Hugo Gutierrez-de-Teran,⁸ Eddy Sotelo,^{3,*} and Andreas Lundqvist^{1,*}

¹Department of Oncology-Pathology, Karolinska Institute, Stockholm SE-17177, Sweden.

²School of Biological Sciences, Nanyang Technological University, Singapore. ³Center for Research in Biological Chemistry and Molecular Materials (CiQUS), University of Santiago de Compostela, Santiago de Compostela ES-15782, Spain. ⁴Singapore Immunology Network SIGN, Agency for Science, Technology and Research, Singapore, Republic of Singapore.

⁵Department of Microbiology, Tumor and Cell Biology, Science for Life Laboratory, Karolinska Institutet, Stockholm, Sweden. ⁶Department of Applied Physics, Science for Life Laboratory, KTH Royal Institute of Technology, Stockholm SE-11419, Sweden. ⁷Center for Research in Molecular Medicine and Chronic Diseases (CiMUS), University of Santiago de Compostela, Santiago de Compostela ES-15782, Spain. ⁸Department of Cell and Molecular Biology, Uppsala University, Uppsala SE-75124, Sweden.

Corresponding authors:

*E.S.: phone, +34-881815732; fax, +34 881815704; e-mail, e.sotelo@usc.es.

*A.L.: phone, +46-(0)8-517 768 59; e-mail, andreas.lundqvist@ki.se.

Table of contents

Supplementary methods and results.....	S2
Molecular dynamics parameters.....	S3
Chemistry.....	S4
Synthetic procedures.....	S5
Supplementary tables	S7
Supplementary figures.....	S8
Spectroscopic and analytical data.....	S16
References.....	S19

Supplementary methods and results

Annexin V viability analysis

Cells were washed with Annexin V binding buffer (BioLegend) then incubated with Alexa Fluor 647 – conjugated Annexin V (BioLegend) at room temperature for 15 minutes. For A_{2A}AR and A_{2B}AR expression profiling, cells were washed with BD Perm/Wash then incubated with BD CytoFix/CytoPerm at 4°C for 20 minutes. The cells were then washed and stained with PE-conjugated A_{2A}AR mouse antibody (Clone 7F6-G5-A2; Santa Cruz Biotechnology, sc-32261 PE) at room temperature for 30 minutes. After washing twice to remove most A_{2A}AR antibody possible, goat A_{2B}AR primary antibody (Clone PA5-18422; Thermo Fisher Scientific) was incubated at 4°C overnight. The cells were subsequently washed and stained with Alexa Fluor 488-conjugated anti-goat secondary antibody (Thermo Fisher Scientific) at room temperature for 1 hour. The cells were then washed with FC buffer twice before acquiring on NovoCyte. A_{2A}AR and A_{2B}AR fluorescence minus one (FMO) staining were also prepared. For differential expression of ADO ectonucleotidases, day five patient-derived sarcoma spheroids were digested and stained for CD45, CD73 and CD39 using the same procedures as cell surface staining (Supplementary Table 1).

Public database bioinformatic analysis

Normalised, batch-corrected, gene expression and DNA copy number of ADORA2B from The Cancer Genome Atlas (TCGA) Pan-Cancer Genome Atlas project (Pan-Can) were accessed and downloaded from USCS Xena Browser (<https://xenabrowser.net>). Fold change of transcript per million was visualized using Gene Expression Profiling Interactive Analysis (GEPIA) Browser (<http://gepia.cancer-pku.cn/>). DNA alteration frequency from TCGA Pan-Can were accessed and visualized in cBioPortal (<https://www.cbioportal.org>).

Chromium (51Cr) release cytotoxicity assay

Chromium (51Cr) release assay was used to measure the autologous TILs-mediated cytotoxicity against the established patient-derived breast and cancer cell lines. Briefly, breast and sarcoma tumor cells were labelled with 51Cr (PerkinElmer) as target cells and seeded on 96-well V-bottom plate (Corning) at 5 000cells/well. Effector TILs were added at the indicated Effector: Target (E:T) ratios. The supernatants were collected carefully into LUMA plates (PerkinElmer) after 24 and 48 hours of co-culture. After drying overnight, radioactivity of the plate was read with MicroBeta2 (PerkinElmer).

Relative adenosine production assay

An ectonucleotidase CD73 assay was optimized to measure the relative ADO production based on competitive AMP blockade and presence of CD73+ cells [47,48]. Day five patient-derived sarcoma spheroids were digested and split into triplicates in X-VIVO20 and 1% PS culture media with an excessive amount of AMP at 0.4mM (Sigma-Aldrich) incubated for 30 minutes. After 1500 RPM was applied for three minutes, 25 μ L supernatant were removed and mixed with 25 μ L of 200 μ M ATP (Sigma-Aldrich) in the same media. 25 μ L of this mixture was added to a white opaque OptiPlate (PerkinElmer) containing 25 μ L Cell-Titer Glo reagent (Promega, US). Relative luminescence unit (RLU) can be read on SPARK 10M plate reader with an integration time of 100ms.

Molecular dynamics parameters.

A 25 \AA sphere centered on the center of geometry of the ligand is considered for MD simulations of each generated protein-ligand complex, in order to equilibrate it from the initial docking pose. Protein atoms in the boundary of the sphere (22-25 \AA outer shell) had a positional restraint of 20 kcal/mol/ \AA^2 , while solvent atoms were subject to polarization and radial restrains using the surface constrained all-atom solvent (SCAAS)¹⁻³ model to mimic the properties of bulk water at the sphere surface. Atoms lying outside the simulation sphere are tightly constrained (200 kcal/mol/ \AA^2 force constant) and excluded from the calculation of non-bonded interactions. Long range electrostatics interactions beyond

a 10 Å cut off were treated with the local reaction field method,⁴ and all titratable residues outside the sphere were neutralized and histidine residues were assigned a hydrogen atom on the δ nitrogen solvent bond and angles were constrained using the SHAKE algorithm.⁵ The OPLS-AA/M force field was used, with compatible ligand parameters generated with the fflid server.⁶ The simulation sphere was warmed up from 0.1 to 298 K, during a first equilibration period of 0.61 nanoseconds, where an initial restraint of 25 kcal/mol/Å² imposed on all heavy atoms was slowly released for all complexes. Thereafter the system was subject to ten parallel replicates of unrestrained MD, of 0.5 ns length each.

Chemistry

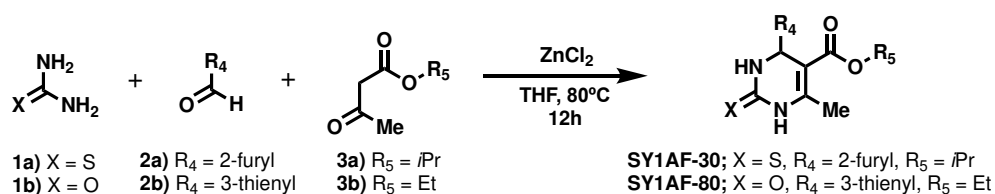
All starting materials, reagents and solvents were purchased and used without further purification. After extraction from aqueous phases, the organic solvents were dried over anhydrous sodium sulfate. The reactions were monitored by thin-layer chromatography (TLC) on 2.5 mm Merck silica gel GF 254 strips, and each purified compound showed a single spot; unless stated otherwise, UV light and/or iodine vapor were used to detect compounds. The reactions were performed in coated Kimble vials on a PLS (6×4) Organic Synthesizer with orbital stirring. Purification of isolated products was carried out by column chromatography (Kieselgel 0.040–0.063 mm, E. Merck).

The purity and identity of all tested compounds were established by a combination of HPLC, high resolution mass spectrometry and NMR spectroscopy. Melting points were determined on a Gallenkamp melting point apparatus and are uncorrected. The NMR spectra were recorded on Bruker AM300 spectrometer. Chemical shifts are given as δ values against tetramethylsilane as internal standard and J values are given in Hz. High-resolution mass spectra (HRMS) were obtained on an Autospec Micromass spectrometer. NMR and HRMS reports of novel compounds are shown at the end of Spectroscopical and analytical data section. The unequivocally assignment of the different regioisomers was assisted by NOE experiments. Routinely purity control was performed by analytical HPLC using a Water Breeze™ 2 (binary pump 1525, detector UV/Visible 2489, 7725i Manual Injector Kit 1500 Series) using an Luna® Silica 100 Å, 4.6 mm × 150 mm, 5 μ m column with gradient elution using hexane/isopropyl alcohol mixture in different percentages as mobile phase. The purity of all tested compounds was determined to be >95%.

The purity and identity of all tested compounds were established by a combination of HPLC, high resolution mass spectrometry and NMR spectroscopy. Melting points were determined on a Gallenkamp melting point apparatus and are uncorrected. The NMR spectra were recorded on Bruker AM300 spectrometer. Chemical shifts are given as δ values against tetramethylsilane as internal standard and J values are given in Hz. A copy of the NMR spectra is found in the supplementary data file. High-resolution mass spectra (HRMS) were obtained on an Autospec Micromass spectrometer. HRMS reports of novel compounds are shown in Supporting information. The unequivocally assignment of the different regioisomers was assisted by NOE experiments. Routinely purity control was performed by analytical HPLC using a Water Breeze™ 2 (binary pump 1525, detector UV/Visible 2489, 7725i Manual Injector Kit 1500 Series) using a Luna® Silica 100 Å, 4.6 mm × 150 mm, 5 μ m column with gradient elution using hexane/isopropyl alcohol mixture in different percentages as mobile phase. The purity of all tested compounds was determined to be $\geq 95\%$.

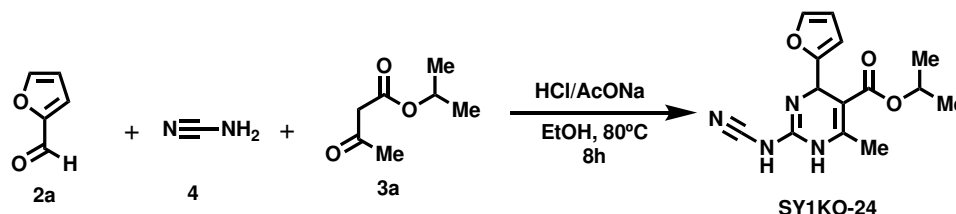
Synthetic procedures

Procedure for the Biginelli synthesis of 3,4-dihydropyrimidin-2(1H)-ones SY1AF-30⁷ and SY1AF-80⁷



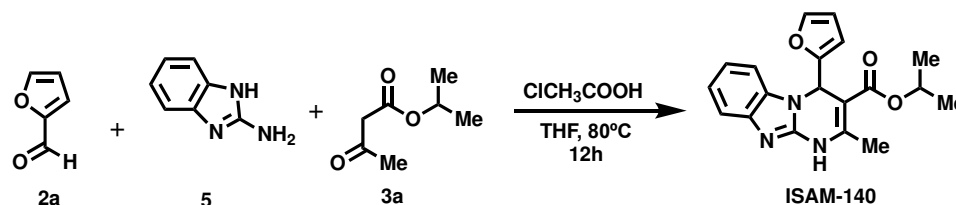
A mixture of the urea **1a** or thiourea **1b** (7.5 mmol), 2-furancarboxaldehyde **1a** or 3-thiophenecarboxaldehyde **1b** (5 mmol), isopropyl **3a** or ethyl **3b** acetoacetate (5 mmol) and ZnCl₂ (0.5 mmol) in 3 mL of THF in coated Kimble vials was stirred with orbital stirring at 80°C for 12h. After completion of the reaction, as indicated by TLC, the reaction mixture was poured onto crushed ice and stirred for 5-10 minutes. The solid separated was filtered under suction, washed with ice-cold water (20 mL), and then purified either by recrystallization or column chromatography on silica gel.

Procedure for the Biginelli synthesis of isopropyl 2-(cyanoimino)-4-(furan-2-yl)-6-methyl-1,2,3,4-tetrahydropyrimidine-5-carboxylate SY1KO-24⁸



A mixture of cyanamide **4** (2 mmol), 2-furanecarboxaldehyde **2a** (1 mmol), isopropyl acetoacetate **3a**, sodium acetate (1 mmol), and concentrated hydrochloric acid (0.5 mL) in 7 mL of ethanol in a coated Kimble vial was stirred by orbital stirring at 80°C for 8h. After completion of the reaction, as indicated by TLC, the reaction mixture was poured onto crushed ice and stirred for 10 min. The solid was filtered under suction, washed with ice-cold water (20 mL) and then purified either by recrystallization or column chromatography on silica gel.

Procedure for the Biginelli synthesis of isopropyl 4-(furan-2-yl)-2-methyl-1,4-dihydrobenzo[4,5]imidazo[1,2-a]pyrimidine-3-carboxylate ISAM-140⁹



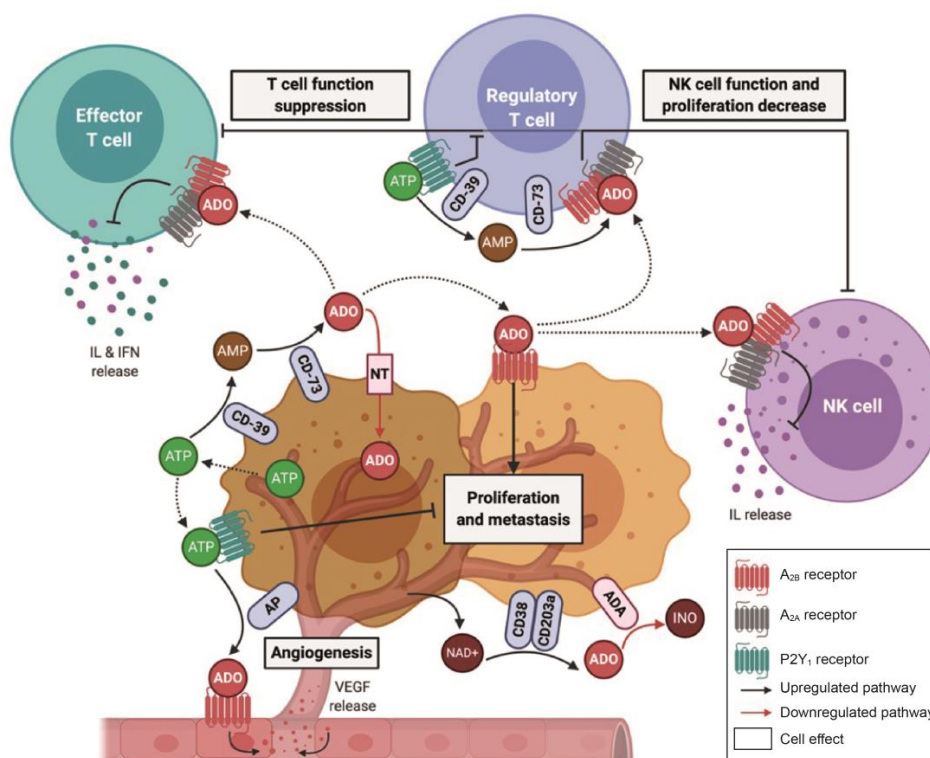
A mixture of 2-aminobenzimidazole **5** (7.5 mmol), 2-furanecarboxaldehyde **2a** (5 mmol), isopropyl acetoacetate **3a** (5 mmol), and 2-chloroacetic acid (0.05 mmol) in 3 mL of THF in coated Kimble vials was stirred with orbital stirring at 80°C for 12h. After completion of the reaction, as indicated by TLC, the reaction mixture was poured onto crushed ice and stirred for 10 min. The solid was filtered under suction, washed with ice-cold water (20 mL) and then purified either by recrystallization or column chromatography on silica gel.

Supplementary tables

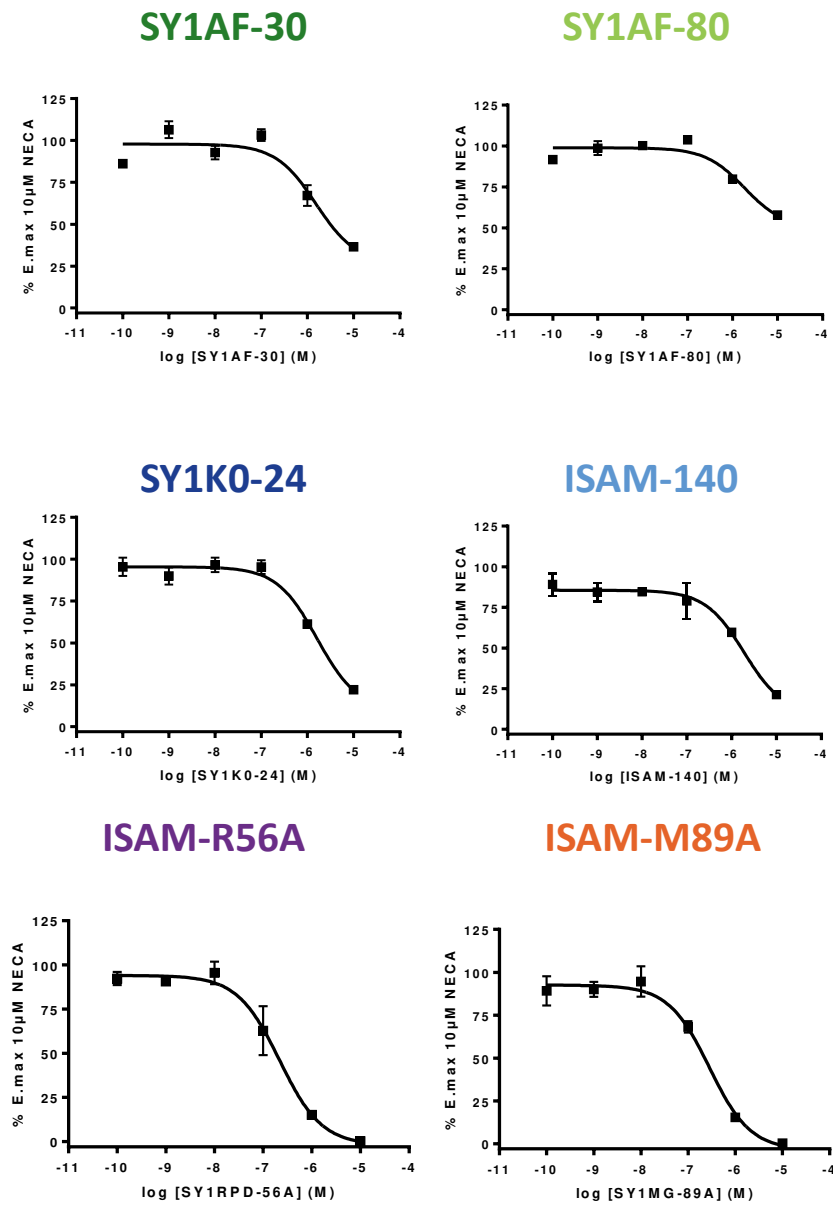
Supplementary Table 1. List of cell surface antibodies used in flow cytometry. A. A_{2A}AR & A_{2B}AR expression profiling **B.** CFSE Proliferation and Annexin V viability assay **C.** ADO ectonucleotidase expression **D.** Spheroid infiltrated TIL phenotyping **E.** Extracellular ADO uptake assay. **F.** IFN γ and Perforin cytokine production assay **G.** Breast tumor resection phenotyping.

Antigen	Conjugate	Distributor	Catalog Number	A	B	C	D	E	F	G
CD3 (T cell)	PerCP/Cy5.5	BioLengend	30429	✓			✓			
	PE-CF594	BD Bioscience	562280		✓			✓	✓	
	Brilliant Violet 650	BD Bioscience	563852							✓
CD4 (T helper cell)	Pacific Blue	BD Bioscience	558116	✓	✓		✓	✓	✓	
	PE	BD Bioscience	555347							✓
CD8 (Cytotoxic T cell)	PE/Cy7	eBioscience	25-0088-42	✓	✓		✓	✓	✓	✓
CD45RA (Naïve T cell)	Brilliant Violet 650	BioLegend	304136	✓	✓					
CD27 (Central memory marker)	Brilliant Violet 605	BioLegend	302830	✓	✓					
CD56 (NK cell)	APC/Cy7	BioLegend	318331	✓						
	Brilliant Violet 570	BD Horizon	564058		✓		✓			
		BioLegend	318330							
CD19 (B cell)	Brilliant Violet 570	BioLegend	302235	✓						
CD45 (Leukocyte)	Brilliant Violet 650	BioLegend	304044			✓				
	PerCP-eFluoro 710	eBioscience	46-0459-42							✓
CD73	APC/Cy7	BioLegend	344022			✓				
CD39	PE/Cy7	BioLegend	328211			✓				
CD11a	PE	BioLegend	301208				✓			
CD49a	APC/Fire 750	BioLegend	328317				✓			
CD69	Brilliant Violet 785	BioLegend	310931				✓		✓	
CD103	APC	BioLegend	350215				✓			
IFN γ	eFluor450	eBioscience	48-7319-42						✓	
Perforin	PE	BioLegend	308106						✓	
CD11b	APC-Cy7	BD Bioscience	557754							✓
CD11c	PE-Cy7	BD Bioscience	561356							✓
CD14	Brilliant Violet 785	BD Bioscience	563698							✓
CD15	Alexa Fluor 488	BioLegend	301910							✓
CD68	PE-CF594	BD Bioscience	564944							✓
HLA-DR	Brilliant Violet 650	BD Bioscience	564231							✓
CD90	APC	BD Bioscience	559869							✓
CD31	Brilliant Violet 421	BD Bioscience	564089							✓
EPCAM	Brilliant Violet 785	BioLegend	324238							✓
Live/Dead marker	Aqua	Thermo Fisher Scientific	L34966	✓		✓	✓			✓
	Near-IR	Thermo Fisher Scientific	L10119		✓			✓	✓	

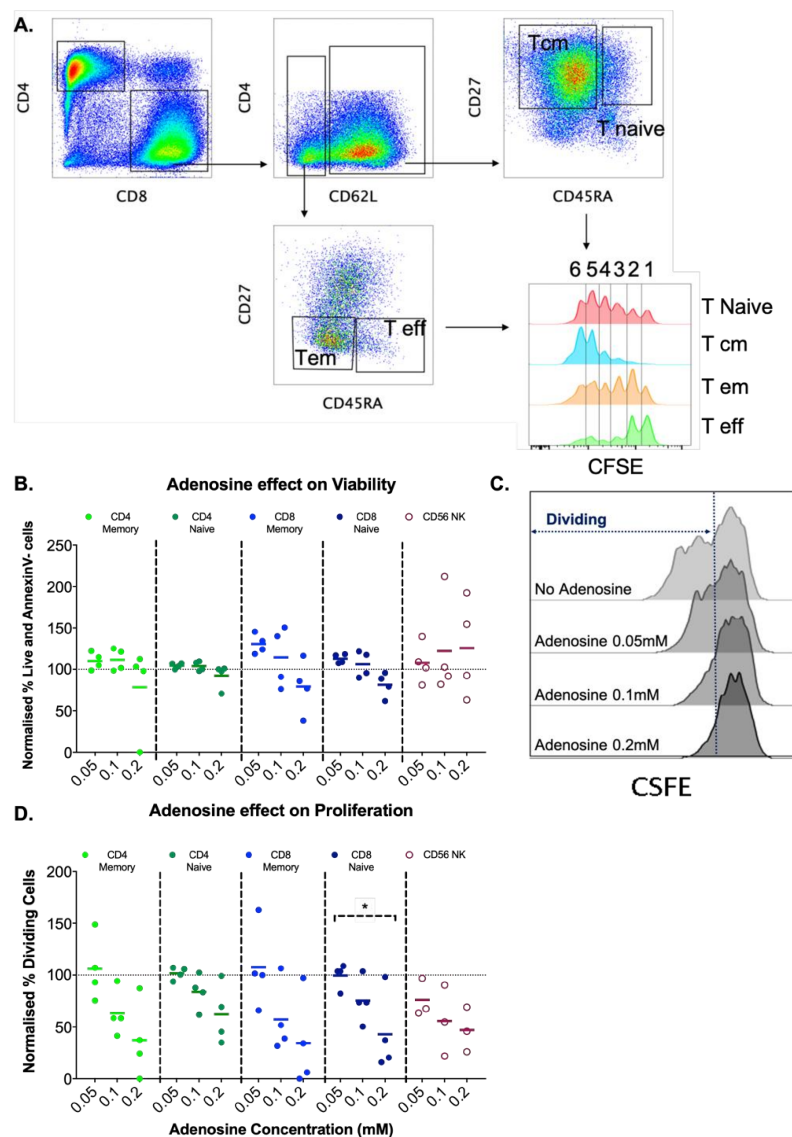
Supplementary figures



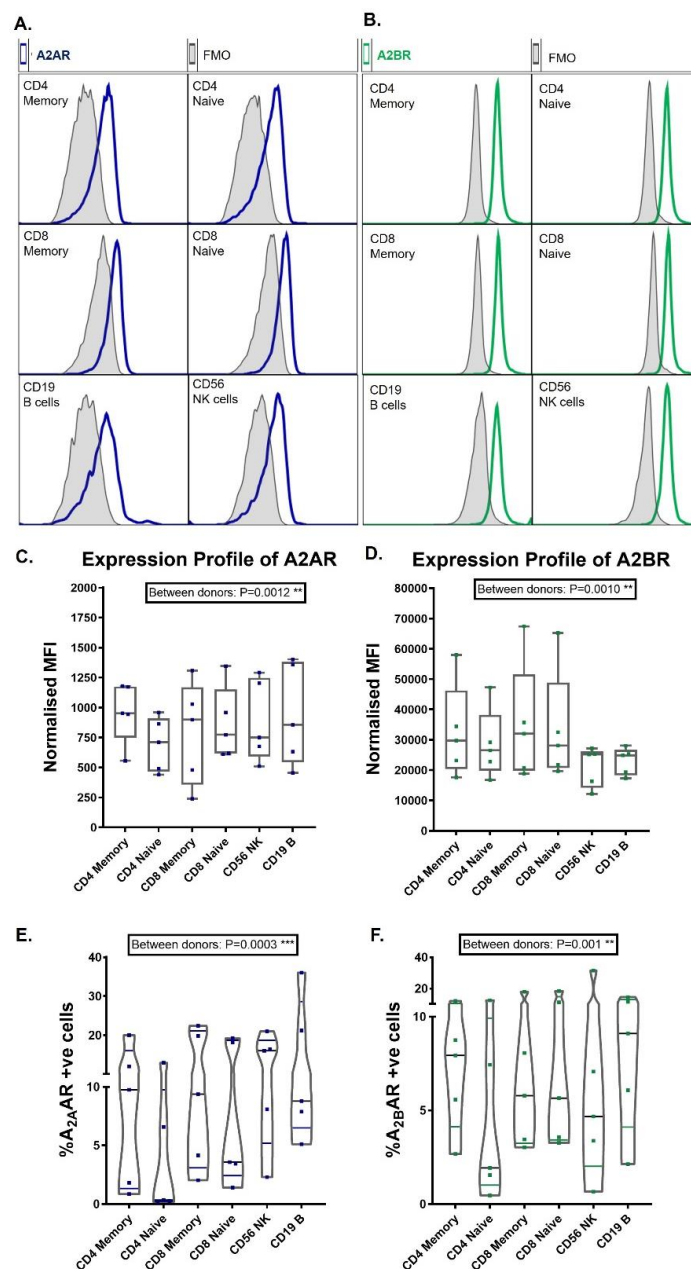
Supplementary Figure 1. Adenosine-mediated effects in the tumor microenvironment (TME). Hypoxia induces the release of ATP and NAD⁺ leading to an increase in the extracellular adenosine (ADO) concentration. The accumulated ATP can either activate P2 purinergic receptors or it can be metabolized by the consecutive action of ectonucleotidases CD39 and CD73 to ADO. Furthermore, NAD⁺ can be transformed to ADO by the CD38/CD203a enzymatic system. The increased ADO concentration is also a consequence of the fact that both ADO reuptake by nucleoside transporters (NT) and adenosine deaminase (ADA) metabolism are downregulated in tumor cells. In the vascular endothelium, ADO interacts with A₂BAR, triggering the release of pro-angiogenic factors like VEGF. Activation of A₂BAR promotes tumor growth and metastasis by increasing cell proliferation, inhibiting apoptosis and reducing cell adhesion. Activation of both A₂A and A₂B ARs by ADO also results in immunosuppressive patterns, downregulating inflammatory cytokine secretion, as well as decreasing the effector function and proliferation of T and natural killer (NK) cells. This figure was created with Biorender.com.



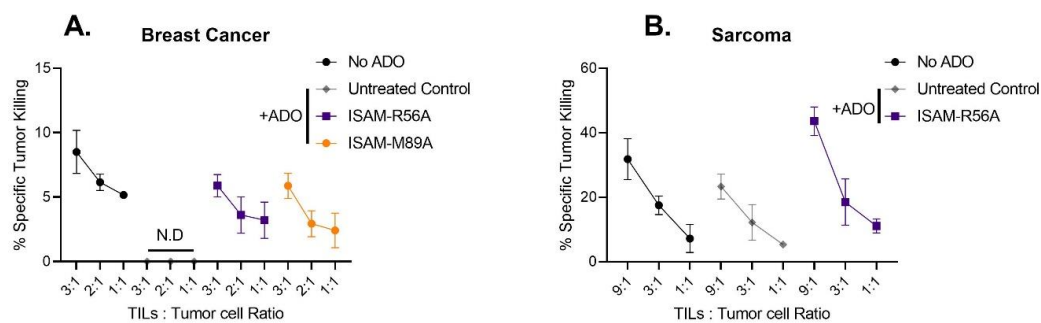
Supplementary Figure 2. Concentration-response curves for cAMP production assay using NECA and test compound.



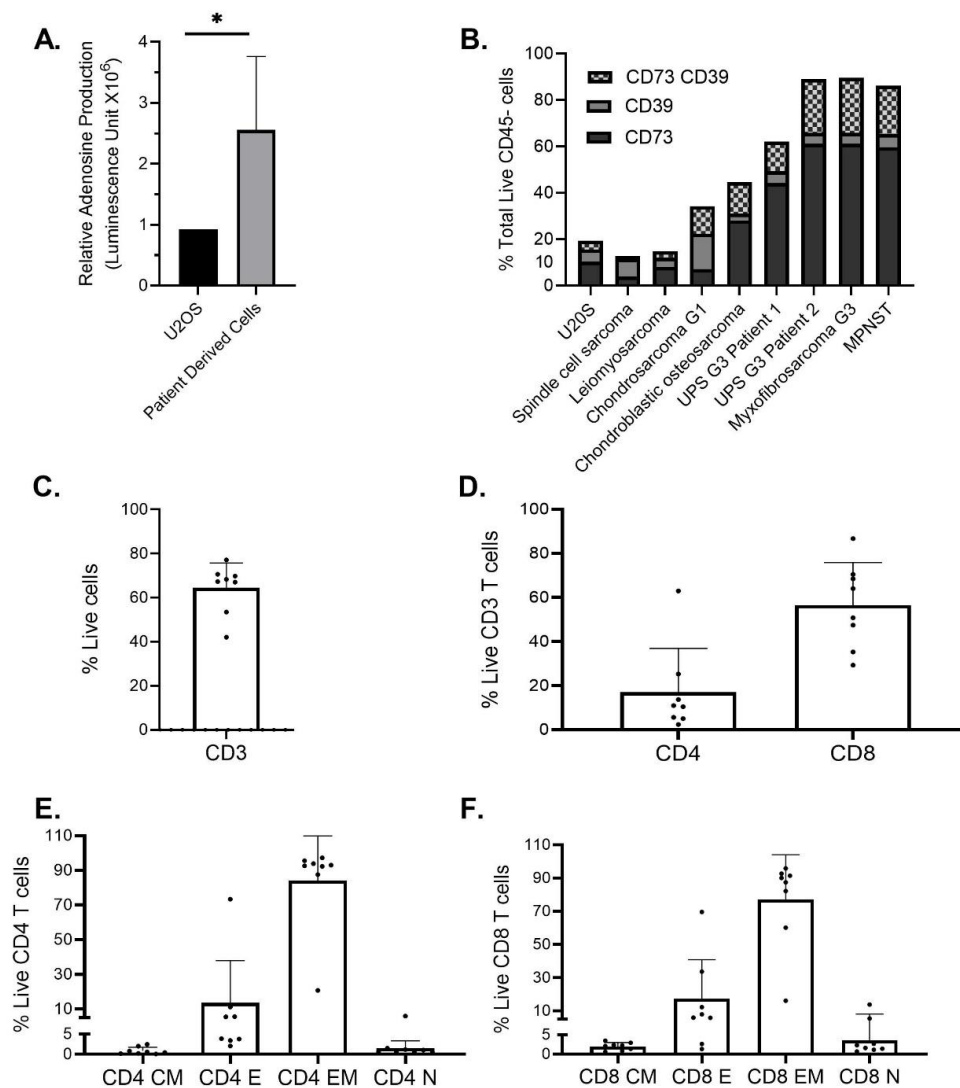
Supplementary Figure 3. Adenosine effects on viability and proliferation in healthy donor peripheral blood T and NK cells. **A.** Representative gating strategies for T cell subsets analyzed by flow cytometry. **B.** Adenosine effect on viability for CD3 T cell subsets and CD56 NK cells after 3-day and 6-day incubation respectively. **C.** Representative CFSE histogram on naïve CD8 T cells dividing cells. **D.** Adenosine effect on proliferation for CD3 T cell subsets and CD56 NK cells after 3-day and 6-day incubation respectively. Normalized percentage to no adenosine suppression (B and D). Mean from 4 different healthy donors are presented. Statistical analysis – 1-way ANOVA (within each cell type) is performed with * $p < 0.05$, ** $p < 0.01$, *** $p < 0.001$ and **** $p < 0.0001$. No statistical significance is not stated. Tcm: Central memory, Tem: Effector memory, Teff: Effector



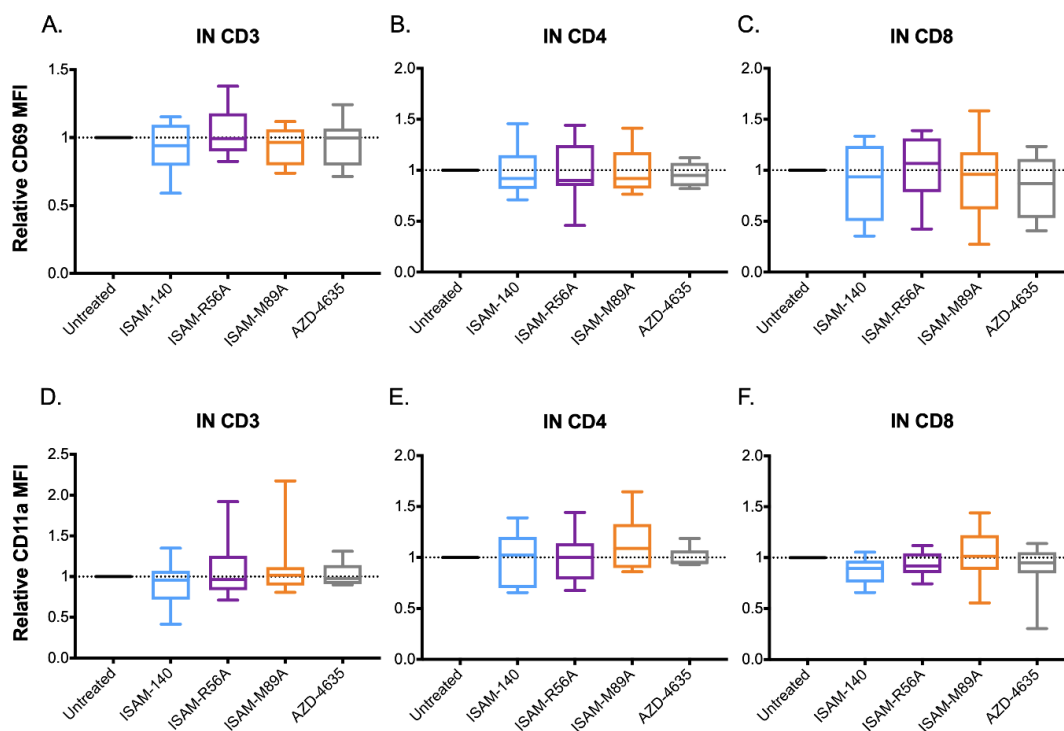
Supplementary Figure 5. Expression profile of A_{2A}AR and A_{2B}AR in healthy donor lymphocyte subsets. Representative histogram of **A.** A_{2A}AR and **B.** A_{2B}AR. Filled histograms show Fluorescence Minus One (FMO) control staining. Expression of **C and E.** A_{2A}AR and **D and F.** A_{2B}AR from healthy donors (n=5). Box plots with minimum, first quartile, median, third quartile, and maximum are presented. Statistical analysis – 1-way ANOVA is performed with * $p<0.05$, ** $p<0.01$, *** $p<0.001$ and **** $p<0.0001$.



Supplementary Figure 6. A. Breast cancer and **B.** Sarcoma TIL-mediated cytotoxicity of autologous tumor cells in the presence or absence of 0.1M synthetic ADO for 48 and 24 hours respectively. ADO: Adenosine, N.D: No difference, E:T ratio: Effector TILs: Target Cancer cells ratio.



Supplementary Figure 7. **A.** Relative adenosine production measured by ectonucleotidase CD73 assay and **B.** differential expression of CD73 and CD39 ectonucleotidases measured by flow cytometry of patient-derived sarcoma spheroids (n=8) and the commercial U2OS 3D culture. Composition of expanded TILs (n=8). Expression of **C.** CD3 **D.** CD4 and CD8 **E.** CD4 T cell subsets and **F.** CD8 T cell subsets. MPNST: malignant peripheral nerve sheath tumors. UPS: Undifferentiated pleomorphic sarcoma. CM: Central Memory, E: Effector, EM: Effector Memory, N: Naïve.



Supplementary Figure 8. Differential expression of relative **A – C.** CD69 and **D – F.** CD11a MFI IN the spheroids (n=8) of CD3, CD8 and CD4 TILs. Antagonist 0.012mM is added.

Spectroscopic and analytical data

(±) **Isopropyl 4-(furan-2-yl)-6-methyl-2-thioxo-1,2,3,4-tetrahydropyrimidine-5-carboxylate (SY1AF-30).**⁷ Yield: 68%. M.p.: 195-196 °C. ¹H-NMR (CDCl₃, 300 MHz), δ (ppm): 7.87 (br s, 1H), 7.33 (d, *J*=1.7 Hz, 1H), 7.22 (br s, 1H), 6.29 (dd, *J*=1.9 Hz, *J*=3.2 Hz, 1H), 6.16 (d, *J*=3.2 Hz, 1H), 5.48 (d, *J*=3.1 Hz, 1H), 5.06-4.99 (m, 1H), 2.37 (s, 3H), 1.23 (d, *J*=6.3 Hz, 3H), 1.12 (t, *J*=6.3 Hz, 3H). ¹³C-NMR (DMSO-*d*₆, 75 MHz), δ (ppm): 165.4, 153.5, 149.1, 144.2, 139.3, 129.7, 109.8, 99.9, 67.1, 46.6, 22.5, 22.3, 18.3. Elem. Anal. calculated for C₁₃H₁₆N₂O₃S, C, 55.70; H, 5.75; N, 9.99; found C, 55.74; H, 5.78; N, 10.02.

(±) **Ethyl 6-methyl-2-oxo-4-(thiophen-3-yl)-1,2,3,4-tetrahydropyrimidine-5-carboxylate (SY1AF-80).**⁷ Yield: 88%. M.p.: 232-233 °C. ¹H-NMR (DMSO-*d*₆, 300 MHz), δ (ppm): 9.17 (br s, 1H), 7.74 (br s, 1H), 7.44 (dd, *J*=3.0 Hz, *J*=5.0 Hz, 1H), 7.13 (d, *J*=2.8 Hz, 1H), 6.98 (dd, *J*=1.2 Hz, *J*=5.0 Hz, 1H), 5.20 (d, *J*=3.4 Hz, 1H), 4.04 (c, *J*=7.0 Hz, 2H), 2.21 (s, 3H), 1.14 (t, *J*=7.0 Hz, 3H). ¹³C-NMR (DMSO-*d*₆, 75 MHz), δ (ppm): 165.5, 152.8, 148.6, 145.9, 126.8, 126.3, 20.9, 99.6, 59.4, 49.6, 17.9, 14.3. Elem. Anal. calculated for C₁₂H₁₄N₂O₃S, C, 54.12; H, 5.30; N, 10.52; found C, 54.15; H, 5.29; N, 11.53.

(±) **isopropyl 2-(cyanoimino)-4-(furan-2-yl)-6-methyl-1,2,3,4-tetrahydropyrimidine-5-carboxylate (SY1KO-24).**⁸ Yield 82%. M.p.: 212-214 °C. ¹H NMR (300 MHz, DMSO-*d*₆) δ (ppm): 10.16 (bs, 1H), 9.09 (bs, 1H), 7.58 (d, *J* = 2.1 Hz, 1H), 6.38 (t, *J* = 2.2, 1H), 6.16 (d, *J* = 3.3 Hz, 1H), 5.29 (d, *J* = 3.9 Hz, 1H), 4.87 (p, *J* = 6.2 Hz, 1H), 2.26 (s, 3H), 1.17 (d, *J* = 6.1 Hz, 3H), 1.07 (d, *J* = 6.0 Hz, 3H). ¹³C NMR (75 MHz, DMSO-*d*₆) δ (ppm): 164.3, 155.7, 154.8, 147.2, 143.2, 116.7, 111.0, 106.9, 99.6, 67.5, 47.7, 22.1, 21.9, 17.7. HRMS (EI) *m/z*: calcd for C₁₄H₁₆N₄O₃ [M]⁺: 288.1222; found: 288.1225.

(±) **Isopropyl 4-(furan-2-yl)-2-methyl-1,4-dihydrobenzo[4,5]imidazo[1,2-*a*]pyrimidine-3-carboxylate (ISAM-140).**⁹ Yield 61%. M.p.: 253–255 °C. ¹H NMR (300 MHz, DMSO-*d*₆), δ (ppm): 10.78 (brs, 1H), 7.67–7.23 (m, 3H), 7.19–6.84 (m, 2H), 6.52 (s, 1H), 6.44 (d, *J* = 3.3 Hz, 1H), 6.37–6.23 (m, 1H), 4.86 (h, *J* = 6.3 Hz, 1H), 2.44 (s, 3H), 1.21 (d, *J* = 6.2 Hz, 3H), 1.05 (d, *J* = 6.1 Hz, 3H). ¹³C NMR (75 MHz, DMSO-*d*₆), δ (ppm): 165.0, 153.3, 148.0, 146.0, 143.0, 142.6, 132.0, 122.3, 120.7,

117.2, 110.8, 110.2, 108.2, 94.9, 67.0, 49.7, 22.3, 22.0, 19.1. HRMS (ESI) m/z : calcd for $C_{19}H_{20}N_3O_3$ $[M + H]^+$: 338.1488; found: 338.7927.

(±) **Isopropyl 1-(2-fluorobenzyl)-4-(furan-2-yl)-2-methyl-1,4-dihydrobenzo[4,5]-imidazo[1,2-a]pyrimidine-3-carboxylate (ISAM-R56A)**. Yield 27%. Mp: 182-183 °C. 1H NMR (300 MHz, $CDCl_3$) δ (ppm): 7.72 – 7.51 (m, 1H, Ar-H), 7.52 (dd, $J = 7.3, 2.0$ Hz, 1H, Ar-H), 7.41 – 7.00 (m, 7H, Ar-H), 6.61 (s, CH), 6.31 (d, $J = 1.7$ Hz, 2H, Ar-H), 5.82 (d, $J = 17.4$ Hz, 1H, $CH_2C_6H_4F$), 5.52 (d, $J = 17.4$ Hz, 1H, $CH_2C_6H_4F$), 5.13 (hept, $J = 6.3$ Hz, 1H, $OCH(CH_3)_2$), 2.64 (s, 3H, CH_3), 1.31 (d, $J = 6.2$ Hz, 3H, $OCH(CH_3)_2$), 1.21 (d, $J = 6.26$ Hz, 3H, $OCH(CH_3)_2$). ^{13}C NMR (75 MHz, $CDCl_3$) δ (ppm): 165.4, 160.5 (d, $J = 246.3$ Hz), 153.0, 148.3, 147.5, 142.2, 141.8, 132.9, 129.1 (d, $J = 8.1$ Hz, Ar-C), 127.8 (d, $J = 3.6$ Hz), 124.6 (d, $J = 3.6$ Hz), 124.3 (d, $J = 13.7$ Hz), 122.6, 121.2, 117.7, 115.5 (d, $J = 21.1$ Hz), 110.3, 109.5, 107.6, 98.9, 67.8, 49.5, 42.5, 22.1, 21.7, 15.8. HRMS (APCI) m/z calcd. for $C_{26}H_{25}FN_3O_3$ $[M+H]^+$: 446.1874; found: 446.1876.

(±) **Isopropyl 10-(2-fluorobenzyl)-4-(furan-2-yl)-2-methyl-1,4-dihydrobenzo[4,5]-imidazo[1,2-a]pyrimidine-3-carboxylate (ISAM-R56B)**. Yield: 38%. Mp: 166-167 °C. 1H NMR (300 MHz, $CDCl_3$) δ (ppm): 7.42 – 7.21 (m, 4H, Ar-H), 7.12 (m, 5H, Ar-H), 6.61 (s, 1H, CH), 6.43 – 6.21 (m, 2H, Ar-H), 5.52 – 5.31 (m, 2H, $CH_2C_6H_4F$), 5.12 (hept, $J = 6.4$ Hz, 1H, $OCH(CH_3)_2$), 2.61 (s, 3H, CH_3), 1.3 (d, $J = 6.3$ Hz, 3H, $OCH(CH_3)_2$), 1.21 (d, $J = 6.3$ Hz, 3H, $OCH(CH_3)_2$). ^{13}C NMR (75 MHz, $CDCl_3$) δ (ppm): 166.3, 160.5 (d, $J = 246.3$ Hz), 160.2, 154.9, 148.9, 141.8, 130.6, 130.1 (d, $J = 3.7$ Hz), 129.7 (d, $J = 8.2$ Hz), 129.2, 124.6 (d, $J = 3.6$ Hz), 122.7 (d, $J = 42.7$ Hz), 115.5 (d, $J = 21.5$ Hz), 110.4, 109.7, 108.8 (d, $J = 2.8$ Hz), 107.7, 95.9, 66.4, 50.4, 38.5 (d, $J = 5.3$ Hz), 24.9, 22.3, 22.0. HRMS (APCI) m/z calcd. for $C_{26}H_{25}FN_3O_3$ $[M+H]^+$: 446.1874; found: 446.1877.

(±) **Isopropyl 8-chloro-4-(furan-3-yl)-2-methyl-1,4-dihydrobenzo[4,5]imidazo[1,2-a]pyrimidine-3-carboxylate (ISAM-M89A)**. Yield: 37%. Mp 256 – 258 °C. 1H NMR (300 MHz, $CDCl_3$), δ (ppm): 11.95 (brs, 1H, NH), 7.48 (s, 1H, Ar-H), 7.38 (s, 1H, Ar-H), 7.25 (s, 1H, Ar-H), 7.06-7.21 (m, 2H, Ar-H), 6.52 (s, 1H, CH), 6.11 (s, 1H, Ar-H), 5.11-5.05 (m, 1H, $OCH(CH_3)_2$), 2.70 (s, 3H, CH_3), 1.35 (d, $J = 6.1$ Hz, 3H, $OCH(CH_3)_2$), 1.31 (d, $J = 6.0$ Hz, 3H, $OCH(CH_3)_2$). ^{13}C NMR (75 MHz, $CDCl_3$), δ (ppm): 165.3, 147.8, 145.6, 142.3, 141.7, 130.3, 128.2, 126.4, 126.1, 122.7, 121.3, 116.3,

110.2, 99.4, 67.8, 52.1, 21.9, 19.5. HRMS (APCI) m/z calcd. for $C_{19}H_{19}ClN_3O_3$ $[M+H]^+$: 372.1109; found: 372.1111.

(±) **Isopropyl 7-chloro-4-(furan-3-yl)-2-methyl-1,4-dihydrobenzo[4,5]imidazo[1,2-a]pyrimidine-3-carboxylate (ISAM-M89B)**. Yield: 35%. Mp 241 – 243 °C. 1H NMR (300 MHz, $CDCl_3$), δ (ppm): 7.38 (m, 2H, Ar-H), 7.06-7.28 (m, 3H, Ar-H), 6.42 (s, 1H, CH), 6.13 (m, 1H, Ar-H), 5.14-4.99 (m, 1H, $OCH(CH_3)_2$), 2.65 (s, 3H, CH_3), 1.37 (d, $J = 6.2$ Hz, 3H, $OCH(CH_3)_2$), 1.26 (d, $J = 6.2$ Hz, 3H, $OCH(CH_3)_2$). ^{13}C NMR (75 MHz, $CDCl_3$), δ (ppm): 165.1, 147.6, 146.0, 143.6, 139.8, 139.7, 132.1, 126.6, 125.3, 123.1, 117.0, 109.7, 108.7, 98.8, 67.8, 48.4, 22.2, 21.9, 19.3. HRMS (APCI) m/z calcd. for $C_{19}H_{19}ClN_3O_3$ $[M+H]^+$: 372.1109; found: 372.1111.

References

- (1) King, G., and Warshel, A. (1989) A surface constrained all-atom solvent model for effective simulations of polar solutions. *J. Chem. Phys.* *91*, 3647. DOI: 10.1063/1.456845.
- (2) Marelius, J., Kolmodin, K., Feierberg, I., Åqvist, J., and Aqvist, J. (1998) Q: a molecular dynamics program for free energy calculations and empirical valence bond simulations in biomolecular systems. *J. Mol. Graph. Model.* *16*, 213–225. DOI: 10.1016/S1093-3263(98)80006-5.
- (3) Mastelic-Gavillet, B., Navarro Rodrigo, B., Décombaz, L., Wang, H., Ercolano, G., Ahmed, R., Lozano, L. E., Ianaro, A., Derré, L., Valerio, M., Tawadros, T., Jichlinski, P., Nguyen-Ngoc, T., Speiser, D. E., Verdeil, G., Gestermann, N., Dormond, O., Kandalaf, L., Coukos, G., Jandus, C., Ménétrier-Caux, C., Caux, C., Ho, P. C., Romero, P., Harari, A., and Vigano, S. (2019) Adenosine mediates functional and metabolic suppression of peripheral and tumor-infiltrating CD8⁺ T cells. *J. Immunother. Cancer* *7*, 1–16. DOI: 10.1186/s40425-019-0719-5.
- (4) Lee, F. S., and Warshel, A. (1992) A local reaction field method for fast evaluation of long-range electrostatic interactions in molecular simulations. *J. Chem. Phys.* *97*, 3100–3107. DOI: 10.1063/1.462997.
- (5) Ryckaert, J.-P. J., Ciccotti, G., and Berendsen, H. J. . H. (1977) Numerical integration of the cartesian equations of motion of a system with constraints: molecular dynamics of n-alkanes. *J. Comput. Phys.* *23*, 327–341. DOI: 10.1016/0021-9991(77)90098-5.
- (6) Kaminski, G. A.; Friesner, R. A.; Tirado-Rives, J.; Jorgensen, W. L. (2001) Evaluation and reparametrization of the OPLS-AA force field for proteins via comparison with accurate quantum chemical calculations on peptides. *J. Phys. Chem.* *105*, 6474–6487. DOI:

10.1021/jp003919d.

(7) Crespo, A., Maatougui, A. El, Biagini, P., Azuaje, J., Coelho, A., Brea, J., Garc, X., and Gutie, H. (2013) Discovery of 3,4-Dihydropyrimidin-2(1H)-ones As a Novel Class of Potent and Selective A2B Adenosine Receptor Antagonists. *ACS Med. Chem. Lett.* *2*, 1031–1036.

DOI: 10.1021/ml400185v.

(8) Carbajales, C., Azuaje, J., Oliveira, A., Loza, M. I., Brea, J., Cadavid, M. I., Masaguer, C. F., García-Mera, X., Gutiérrez-De-Terán, H., and Sotelo, E. (2017) Enantiospecific Recognition at the A2B Adenosine Receptor by Alkyl 2-Cyanoimino-4-substituted-6-methyl-1,2,3,4-tetrahydropyrimidine-5-carboxylates. *J. Med. Chem.* *60*, 3372–3382. DOI:

10.1021/acs.jmedchem.7b00138.

(9) El Maatougui, A., Azuaje, J., González-Gómez, M., Miguez, G., Crespo, A., Carbajales, C., Escalante, L., García-Mera, X., Gutiérrez-De-Terán, H., and Sotelo, E. (2016) Discovery of Potent and Highly Selective A2B Adenosine Receptor Antagonist Chemotypes. *J. Med. Chem.* *59*, 1967–1983. DOI: 10.1021/acs.jmedchem.5b01586.

A_{2B} Adenosine Receptor Antagonists Rescue Lymphocyte Activity in Adenosine-Producing Patient-Derived Cancer Models

Authors

Apple Tay Hui Min, Rubén Prieto-Díaz, Shiyong Neo, Le Tong, Xinsong Chen, Valentina Carannante, Björn Önfelt, Johan Hartman, Felix Haglund, Maria Majellaro, Jhonny Azuaje, Xerardo Garcia-Mera, Jose M. Brea, Maria I. Loza, Willem Jaspers, Hugo Gutierrez-de-Teran, Eddy Sotelo and Andreas Lundqvist

Correspondence

e.sotelo@usc.es
andreas.lundqvist@ki.se

In Brief

A_{2B} Adenosine Receptor (A_{2B}AR) and dual A_{2A}/A_{2B} Adenosine Receptor antagonists rescue T and NK cell proliferation, cytokine production and reduced the tumor growth enhanced by adenosine (ADO) in ADO-producing patient derived cancer models.

